Capture of I^{131} from medical-based wastewater using the highly effective and recyclable adsorbent of g-C$_3$N$_4$ assembled with Mg-Co-Al-layered double hydroxide

Enayatolah Yazdankish[a,*], Maryam Foroughi[b,c], Mohammad Hossein Ahmadi Azqhandi[a,*]

[a] Applied Chemistry Department, Faculty of Gas and Petroleum (Gachsaran), Yasouj University, Gachsaran, 75813-56001, Iran
[b] Department of Environmental Health Engineering, School of Health, Torbat Heydariyeh University of Medical Sciences, Torbat Heydariyeh, Iran
[c] Health Sciences Research Center, Torbat Heydariyeh University of Medical Sciences, Torbat Heydariyeh, Iran

GRAPHICAL ABSTRACT
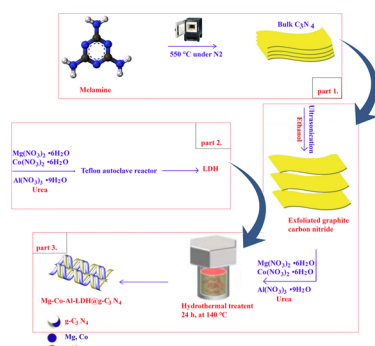
ARTICLE INFO

ABSTRACT

This paper reports a very high capacity and recyclable Mg-Co-Al-layered double hydroxide@ $g - C_3N_4$ nano-composite as the new adsorbent for remediation of radioisotope-containing medical-based solutions. In this work, a convenient solvothermal method was employed to synthesize a new nano-adsorbent, whose features were determined by energy dispersive X-ray (EDS/EDX), XRD, FESEM, TEM, TGA, BET, and FT-IR spectroscopy. The as-prepared nano-adsorbent was applied to capture the radioisotope iodine-131 mainly from the medical-based wastewater under different conditions of main influential parameters, (i.e. adsorbent dose, initial I_2 concentration, sonication time, and temperature). The process was evaluated by three models of RSM, CCD-ANFIS, and CCD-GRNN. Furthermore, comprehensive kinetic, isotherm, thermodynamic, reusability cycles and optimization (by GA and DF) studies were conducted to evaluate the behavior and adsorption mechanism of I_2 on the surface of Mg-Co-Al-LDH@ $g - C_3N_4$ nanocomposite. High removal efficiency (95.25%) of ^{131}I in only 30 min (i.e. during 1/384 its half-life), along with an excellent capacity that has ever been reported (2200.70 mg/g) and recyclability (seven times without breakthrough in the efficiency), turns the nanocomposite to a very promising option in remediation of ^{131}I-containing solutions. Besides, from the models studied, ANFIS described the process with the highest accuracy and reliability with $R^2 > 0.999$.

---

* Corresponding authors.
  E-mail addresses: enayat.yazdankish@yahoo.com (E. Yazdankish), m.ahmadi@yu.ac.ir, mhahmadia58@gmail.com (M.H.A. Azqhandi).

1. Introduction

Medical applications are perhaps the main widespread source of iodine-131 (^{131}I) entrance into the environment. ^{131}I is known as the most widely administrated radiopharmaceutical in nuclear medicine for both therapeutic and diagnostic considerations, mainly to cure hyperthyroidism and thyroid cancer. In developed countries, the average treatment cases of hyperthyroidism and thyroid cancer are estimated to be 150 per million and 38 per million, respectively (Rose et al., 2012; Bahamonde et al., 2017). In fact, following elimination of the whole thyroid gland (thyroidectomy), as the standard treatment protocol for thyroid cancer, radioiodine therapy using 1110–7400 MBq ^{131}I, depending on risk stratification of the patients, is recommended. Moreover, the radiation dosage for hyperthyroid treatments is 100–1000 MBq (Yeyin et al., 2016). Approximately 70% of the administered dose is excreted from the body via urine and then flowed into the wastewater-related facilities, (Montenero et al., 2017). The half-life times radioactive isotopes of iodine differ from around 8 days for ^{131}I to 1.6×10^7 years for ^{129}I. Unfortunately, accumulation of radioactive iodine in our body may increase risk of thyroid cancer, leukemia, as well as metabolic disorders (Zhang et al., 2017). Thus, effectively preventing the spread of the ^{131}I wastes along with adopting the appropriate and innovative strategies for its removal from aqueous solutions are of great importance worldwide (Bo et al., 2013).

In an ^{131}I-containing solution, the iodine species exist in the forms I^- and either I (V) or IO_3^-. The capture of iodine from these environments has been stated to be achievable mainly by two pathways of precipitation by using metal cations M^{n+}, e.g. Hg^{2+} or Pb^{2+} to form precipitates MI$_n$ and adsorption (Liu et al., 2016). The key requirement for the latter is that the introduced and/or developed materials should adsorb radioactive ions not only efficiently but also irreversibly and selectively (Mu et al., 2017). So far, different adsorbents including minerals (Zhang et al., 2013; Kaplan et al., 2000); hydrated aluminum silicates - (Warchoł et al., 2006; Osmanlioglu, 2006) and nanocomposites of silver (Hoskins et al., 2002; Sanchez-Polo et al., 2007; Yang et al., 2011); compounds of lead (II) (Kodama, 1999), mercury (II) (Balsley et al., 1996), and layered double hydroxides (LDHs) have been tried for remediation of radioactive-containing solutions (Kentjono et al., 2010; Ma et al., 2014). In addition, graphitic carbon nitride ($g - C_3N_4$) has been used to capture radioactive element such as Eu (III), Nd (II), and Th (IV) (Liao et al., 2018).

The g-C$_3$N$_4$ is a new form of 2D metal free organic polymer-like material. Owing to the exceptional characteristics including both chemical and thermal stability, non-toxicity, narrow band gap (i.e., 2.7 eV), and ability to interact with toxic molecules selectively, $g - C_3N_4$ have attracted an increasing research attention (Tonda and Jo, 2018). Nevertheless, when employed as the unique adsorbent, $g - C_3N_4$ has shown low adsorption efficiency for different pollutants, probably because of the hydrophobic surface with less functional groups (Liu et al., 2017). Integration of different functional groups through chemical modification could enhance the binding sites of pristine $g - C_3N_4$ (Zou et al., 2016). As mentioned before, LDHs have been used to remediation of radioactive-containing wastewaters successfully. However, the stability of LDHs especially in acidic environments makes them to a controversial option in scaling up the results (Zou et al., 2017). Introduction of LDH into the structure of $g - C_3N_4$ can be a promising amendment option to overcome the mentioned shortcomings of both materials when used individually (Salehi et al., 2018). In fact, LDHs are a type pf host-guest materials with the chemical structure of $[M_{1-x}^{2+} M^{3+}_x (OH)_2]^{x+} A^{n-}_{x/n} . yH_2O$, where M^{2+} and M^{3+} are di- and trivalent metal cations, respectively, and A^{n-} are exchangeable gallery anions (Sepehr et al., 2014). The existence of large interlayer spaces along with the significant number of exchangeable anions, make LDHs to potentially appropriate options to utilize as both ion-exchangers and adsorbents (Abdolmohammad-Zadeh et al., 2013).

It has been convincingly demonstrated that multivariate statistical techniques are advantageous to their classical counterpart (i.e. univariate method) mainly from standpoints of identification of the optimal factors' combination above and beyond of cost- and time-effectiveness (Bingöl et al., 2012). Response surface methodology (RSM) is applied to design of experiments which the obtained results are then based to approximate the coefficients of a mathematical model, to anticipate the response, and to evaluate the adequacy of the developed model (Samarghandi et al., 2016). More recently, simultaneous applying of RSM and intelligent models e.g. random forest (RF) (Azqhandi et al., 2017), adaptive Neuro fuzzy inference system (ANFIS) (Omidi et al., 2018), least squares support vector machines (LS-SVM) (Asfaram et al., 2016), and artificial neural network (ANN)-based (Azqhandi and Shekari, 2018) approaches has attracted considerable attention for both modeling and optimization purposes in (waste)water remediation processes (Geyikçi et al., 2012). The generalized regression neural network (GRNN), as a type of radial basis function NN, and ANFIS, as the combination of ANN and Fuzzy Logic, are two new promising approaches that should be taken more into account for the mentioned processes. Since the former has a good nonlinear approximation capability, an exceptional performance of anti-interference, an autonomous learning capability, and fast convergence rate; and the latter has kept advantages of its parents, they considered as two of the most efficient approaches (Hu et al., 2017; Mostafaei et al., 2016) that are rarely used each other in coupling with RSM to express the relation between eff;ective parameters for adsorption processes.

This study aimed, therefore, to investigate the effect of $g - C_3N_4$ coupled with Co-Ca-Al-layered double hydroxide ($Mg - Co - Al - LDH - g - C_3N_4$) on ^{131}I removal from synthetic medical wastewater. The goal was achieved by the subsequent following steps: (i) the adsorbent ($Mg - Co - Al - LDH - g - C_3N_4$) was synthesized, characterized, and utilized to remove ^{131}I from aqueous media; (ii) the process were evaluated through its modeling using RSM, GRNN, and ANFIS approaches by considering the influence of Initial I$_2$ concentration, adsorbent dose, tempreature, and sonication time; (iii) the models were compared in terms of anticipation and generalization abilities, sensitivity analysis, and optimization performance in ^{131}I removal from synthetic medical wastewater; (iv) the supplementary evaluation of kinetics and isotherm models, thermodynamics, regeneration, and reusability were conducted to facilitate scaling-up the process.

2. Materials and methods

2.1. Apparatuses and chemicals

All chemicals used in this study were analytical pure grade. Mg (NO$_3$)$_2$.6H$_2$O, Co(NO$_3$)$_2$.6H$_2$O, and Al(NO$_3$)$_3$.9H$_2$O were from Sigma Aldrich (Sigma Aldrich, Missouri, USA) and the other chemicals were purchased from Merck ® (Merck KGaA, Darmstadt, DE). The distilled water was used for preparation of all solutions under ambient conditions. The pH of the samples was adjusted using pH meter model-686 (Metrohm, Switzerland, Swiss). A Jasco UV–Vis spectrophotometer V-530 (Jasco, Sapporo, Japan) was utilized to measure I$_2$ concentrations at a predetermined maximum wavelength ($\lambda_{max} \sim 287$ nm). The morphology of the synthesized $g - C_3N_4$, Mg-Co-Al, and Mg - Co - Al - LDH - $g - C_3N_4$ -NC was checked via Scanning Electron Microscope (SEM, Hitachi S-4160) and transmission electron microscopy, (TEM, JEOL JEM-100S). FTIR analyses were recorded on a Buker Tensor 27 FT-IR spectrophotometer. The thermogravimetric analysis (TGA) was conducted by a Perkin Elmer-USA with a heating rate of $10 °C min^{-1}$ in a nitrogen purging atmosphere. The X-ray diffraction patterns (XRD) were conducted using a PANalytical X'Pert PRO PW3040, X-ray diffractometer (PANalytical, Almelo, the Netherlands). The Tecno-GAZ SPA UltraSonic System (Parma, Italy) at frequency and power of 40 kHz and 130 W, respectively, was employed to enhance adsorption of I$_2$ on the synthesized nanocomposite.
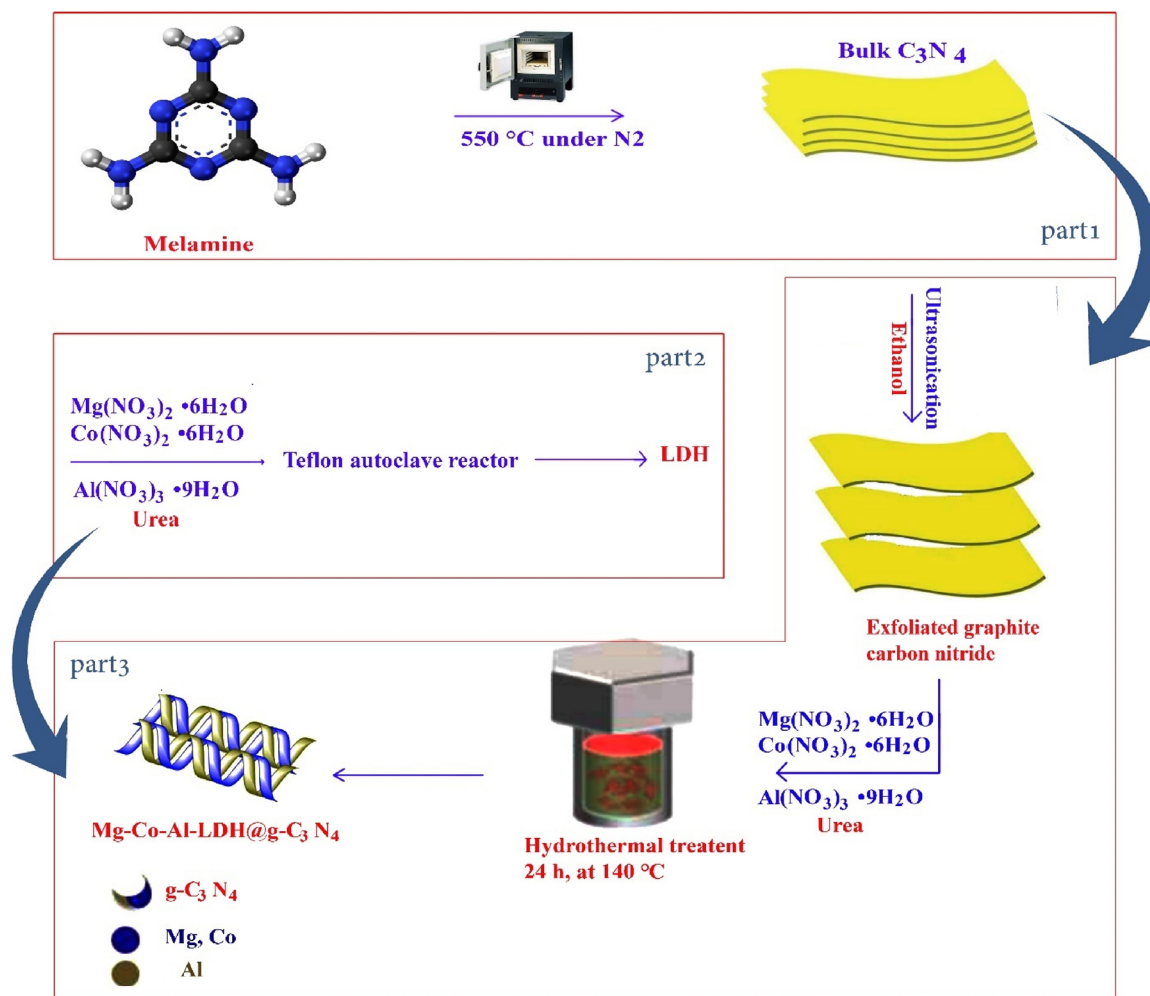
Fig. 1. The synthesis's procedure scheme.

2.2. Fabrication of Mg− Co− Al− LDH− g − C_3N_4

2.2.1. Preparation of g − C_3N_4

The **g − C_3N_4** was fabricated by a thermal condensation (Gao et al., 2017). Specifically, 10 g melamine powder (99%, Sigma Aldrich) was calcined at 550 °C for 3 h in the protection of N_2 gas. Afterward, the heated alumina crucible was cooling down to ambient temperature and obtained light-yellow g-C_3N_4 powder was collected and ground into powder (Yuan et al., 2019) (part 1., Fig. 1).

2.2.2. Preparation of Mg-Co-Al-LDH

The Mg-Co-Al-LDH was synthesized through a solvothermal method. At the first, $Mg(NO_3)_2.6H_2O$, $Co(NO_3)_2.6H_2O$, and Al $(NO_3)_3.9H_2O$ with molar ratio Mg/Co/Al = 3:2:1 (mol/mol/mol) were introduced into 40 mL ethanol. Afterward, 40 mmol urea was added into as-prepared metal solution. The obtained solution was then transferred into a Teflon autoclave reactor and heated at 140 °C for 24 h (Sanati and Rezvani, 2019) (part 2., Fig. 1).

2.2.3. Preparation of Mg− Co− Al− LDH@ g − C_3N_4 - NC

A definite amount of g-C_3N_4 nano-sheet was exfoliated in the 20 mL ethanol by ultrasonication, added to the above-mentioned ethanol-based Mg^{2+}, Co, and AL^{3+} solution. The resulting solution was then mixed with 40 mmol urea, transferred to the autoclave, and heated at 140 °C for 24 h. Ultimately, the suspension was cooled to ambient temperature and the nanocomposite was purified by centrifugation and washed three times with a mixture of ethanol and distilled water. The

produced nanocomposite was dried under vacuum at 75 °C (part 3., Fig. 1).

2.3. Experimental framework

Central composite design (CCD) is perhaps the most powerful and efficient approach under RSM due to providing high accuracy antici-pations of linear and quadratic interactions of factors affecting the process (Witek-Krowiak et al., 2014). This approach is demonstrated as an effective tool in water-based processes modeling and/or optimiza-tion (Folens et al., 2017). The CCD consists of fractional factorial points (labeled as +1, -1), a center point which belongs to the middle level of the factors (labeled as 0), and axial or star points in which the ex-perimental points are located at the distance of α from the center that calculated by $(N_f)^{\frac{1}{4}}$. Therefore, in CCD approach the number of ex-periments is obtained as N = k^2 + 2k + cp, where k indicates the number of studied parameters and cp implies on the replication number of the center point (Dejaegher and Heyden, 2011).

In this study, the effect of four most important factors found from literatures i.e. Mg− Co− Al− LDH@ g− C_3N_4 -NC dose (X_1), initial I_2 concentration (X_2), temperature (X_3), and sonication time (X_4) was investigated through a design framework developed by CCD. Accordingly, The CCD-developed matrix of 30 experiments was based to build the model using Statistica 12.5 (Stat-Ease, USA) software package. The factors contributed as well as the experimental design with five replicates in center point are summarized in Table. 1. The following second order polynomial model was implemented on the

Table 1

The variables, their levels, and the CCD-developed matrix as experimental framework.

Variable	Code	Unit	Levels				
			- α (-1.68)	Low (−1)	Center (0)	High (+1)	+α (+2)
Adsorbent dose	X_1	mg	1	4	7	10	13
Initial I_2 concentration	X_2	mg/L	50	100	150	200	250
tempreature	X_3	ºC	30	35	40	45	50
Time	X_4	min	15	20	25	30	35

		Independent variables				
Std	Run	X_1: Adsorbent dose	X_2: Initial I_2 Concentration	X_3: Temperature	X_4: Time	actual
		4	100	45	20	58.25
2	10	10	100	35	20	53.07
3	3	1	150	40	25	80.55
4	19	7	150	40	15	69.21
5	1	7	150	30	25	62.13
6	8	7	150	40	25	67.55
7	5	4	200	35	20	83.52
8	16	7	150	40	25	66.96
9	15	4	200	35	30	89.74
10	27	7	150	50	25	82.2
11	13	10	100	45	20	73.17
12	14	7	150	40	25	66.66
13	20	10	100	35	30	33.39
14	7	4	100	35	20	62.64
15	25	10	100	45	30	61.85
16	9	7	150	40	25	68.25
17	21	7	250	40	25	84.32
18	2	7	150	40	35	60.29
19	11	7	150	40	25	63.35
20	28	10	200	45	30	83.51
21	30	4	200	45	30	90.23
22	12	10	200	35	30	64.39
23	6	13	150	40	25	73.36
24	29	7	50	40	25	49.03
25	23	10	200	35	20	74.72
26	4	7	150	40	25	67.23
27	17	4	200	45	20	77.84
28	26	4	100	45	30	65.51
29	18	10	200	45	20	82.4
30	22	4	100	35	30	62.82

obtained responses from the designed framework by CCD and was based to anticipate the relationship between all variables along with their effect on the studied process:

$$Y = \underbrace{b_0}_{\text{constant}} + \underbrace{\sum_{i=1}^{k} b_i X_i}_{\text{single terms}} + \underbrace{\sum_{i=1}^{k} b_{ii} X_i^2}_{\text{square terms}} + \underbrace{\sum_{i=1}^{k-1} \sum_{j=i+1}^{k} \beta b_i X_i X_j}_{\text{interaction terms}} + \underbrace{\varepsilon}_{\text{residual}}$$

(1)

where

Y is the anticipated I_2 capture response by the model (R%).

X_i and X_j are the independent variables.

b_0 b_i, b_{ii} and b_{ij} are the intercept, linear, quadratic, and interaction coefficients, respectively.

k refers to the number of parameters.

ε refers corresponds to the model error.

Adequacy of the fitted model was validated using analysis of variance (ANOVA) by evaluating the *p*-value and *F*-value at 95 % confidence limit on top of the axillary confirmative approaches. The developed model's goodness of fit was assessed by the coefficient of determination (R^2), adjusted coefficient of determination (R^2_{adj}), predicated coefficient of determination (R^2_{pred}) and adequate precision (AP). The individual and interaction effects of the parameters on the response were visualized by three-dimensional (3D) plots. The Desirability function (DF) is applied to reach a response with maximum desirability, d_i, (from both technical considerations and attainability point of views) under the specified condition of the parameters

contributed. For the fully undesirable and completely desirable responses d_i is zero and one, respectively (Foroughi et al., 2018a, b).

2.4. Ultrasound-integrated adsorption process

The ultrasound-integrated adsorption experiments were conducted based on the CCD-developed matrix (Table 1). In general, various concentrations of ^{131}I were obtained by dilution of the stock and adjusted for desired pH by either NaOH or HCl 0.1 M. Each solution was then transferred into an aluminum foil covered flask, subjected to the desired dosage of the adsorbent, and ultrasonicated at 40 Hz under a certain temperature and time interval according to that prescribed in experimental matrix. Finally, the nano-composite was removed from the solution with centrifuging at 5000 rpm for 10 min and the supernatant was measured for final concentration of ^{131}I. The amount of I_2 adsorbed on the nano composite at equilibrium was considered as response and was calculated according to Eq. (2) (Azad et al., 2016). The experimentally achieved data from this step was applied to develop the models.

$$R \% = \frac{(C_i - C_f)}{C_i} \times 100$$

(2)

Where C_i and C_f are the I_2 concentrations at time 0 and t, respectively.

2.5. GRNN

GRNN is a normalized radial basis function network which in a hidden neuron is located at the center of all training data. Therefore, the relationship between the dependent and independent factors is approximated from estimating the function directly from the training data instead of assuming a specific functional form. GRNN is advantageous to conventional neural network in running with less additional data without requiring any trial and error optimization process, which in turn ensures a high speed training process as well as more satisfactory results (Panda et al., 2015). Besides, there is only smoothing parameter (σ) that must be adjusted in this method. The excellent performance and simplicity from both structural and implementation standpoints, turns GRNN to an attractive option for real hardware implementation, mainly when the relationship between the dependent and independent variables is not clearly recognized and/or entirely simple. In this study, different σ values between 0.01 and 3.5 were assigned in the training series, whose optimal amount was considered as minimum RMSE (Omidi et al., 2017).

2.6. ANFIS

ANFIS is an artificial intelligence algorithm which in neural network (NN) has been integrated with fuzzy logic. Therefore, this approach benefits of advantages of the parents including learning and optimization capabilities, and connectionist structures from NN; and humanlike 'IF-THEN' rule thinking and ease of incorporating expert knowledge from fuzzy inference system (FIS). This strategy, therefore, can be applied appropriately to solve complex and even extremely nonlinear problems (Aghdam et al., 2016; Najafzadeh et al., 2016), for example in circumstances where there is no practical way to choice memberships and other parameters. The membership function parameters of the embedded FIS in ANFIS are adjusted using either a feed forward backpropagation algorithm alone or integrated with a least square sterategy (Najafzadeh et al., 2016).

In this work the ANFIS architecture which in the Takagi–Sugeno fuzzy type is employed as FIS was used. Although the ANFIS construction and learning procedure has been described in (Jang, 1993), it briefly consists of:

- Layer # 1 (or input layer): to convert of input factors into the fuzzy.
- Layer # 2 (or rule layer): to create fuzzy rules (FR).
- Layer # 3 (or membership function, MF, layer): to normalize the MFs.
- Layer # 4 (or Fuzzy inference (FI) layer): to weight the incoming rules.
- Layer # 5 (or final output layer): to computes the overall output.

It should be note that the input and FI layers in the structure are known as the adaptive layers (Khuntia and Panda, 2012). The modeling process by ANFIS is tuning the design space to attain the lowest error which in, the number and type of MFs for inputs will be adopted and the type of the output MF (either constant or linear) will be adjusted (Pooralhossini et al., 2018). In this study, Fuzzy Logic toolbox (Version 2.3.1.) of MATLAB (The Mathworks, Inc. version R2014b) was used to construct the ANFIS. After examine the mentioned models on this work's experimental data, their performance was comparatively assessed by the listed statistics in Table 2.

2.7. GA

GA is a stochastic and evolutionary algorithm applied to solve an optimization problem through random searches (Askari et al., 2017). The search to find the best fitness is performed through the following iterative cycle: reproduction, selection, crossover, mutation, evaluation for fitness, and stop decision (Enayatifar et al., 2014). In each cycle, the

Table 2
The statistics contributed for performance evaluation of each model.

The statistic	Unit	definition	Equation
R^2		coefficient of determination	$R^2 = 1 - \sum_{i=1}^{n} \left(\frac{(\hat{y}_i - y_{exp,i})^2}{(\hat{y}_i - y_m)^2} \right)$
RMSE		root mean square error	$RMSE = \sqrt{\frac{\sum_{i=1}^{n}(\hat{y}_i - y_i)^2}{N}}$
MSE		mean squared error	$MSE = \frac{1}{N} \sum_{i=1}^{N} (\hat{y}_i - y_i)$
MAE		mean absolute error	$MAE = \frac{\sum_{i=1}^{n} |\hat{y}_i - y_i|}{n}$
AAD			$AAD\% = \left(\frac{1}{n} \sum_{i=1}^{n} (\frac{\hat{y} - y_i}{y_i}) \right) \times 100$
SSE		sums of squares error	$SSE = \sum_{i=1}^{N} (\hat{y}_i - y_i)^2$
SAE		sum of the absolute error	$SAE = \sum_{i=1}^{N} |\hat{y}_i - y_i|$
ARE		average relative error	$ARE = \frac{100}{N} \sum_{i=1}^{N} \frac{|\hat{y}_i - y_i|}{y_i}$
HYBRID		hybrid fractional error function	$HYBRID = \frac{100}{N-P} \sum_{i=1}^{N} \frac{(\hat{y}_i - y_i)^2}{y_i}$
MPSD		Marquart's percentage standard deviation	$MPSD = 100 \sqrt{\frac{1}{N-P} \sum_{i=1}^{N} \frac{(\hat{y}_i - y_i)^2}{y_i}}$
χ^2		Pearson's Chi–square measure	$\chi^2 = \sum_{i=1}^{N} \frac{(\hat{y}_i - y_i)^2}{y_i}$

Table 3
Comparison of optimum degradation percentage from CCD-DF and CCD-GA for I_2.

Factors	Models	
	CCD-DF	CCD-GA
$I_2 (mg\ L^{-1})$	250.00	250.0
Temperature	50.00	47.00
Adsorbent dose (g)	0.013	0.012
Sonication time (min)	35.00	30.00
R%	90.23	95.54

Table 4
Isotherm parameters for I_2 adsorption (initial I_2 concentration = 50.00-250.00 $mg\ L^{-1}$, adsorbent dose = 12.00 mg, Temperature = 47.00 °C, Sonication time = 30.00 min).

Isotherm	Parameters	For TCS removal
Langmuir	$q_{max} (mg\ g^{-1})$	2200.70
$\frac{C_e}{q_e} = \frac{1}{q_m K_L} + \frac{C_e}{q_m}$	$K_L (L\ mg^{-1})$	0.0685
	R_L	0.061-0.142
Plot: $\frac{C_e}{q_e}$ Vs C_e	R^2	0.9986
	X^2	0.2154
Freundlich	$1/n$	0.8345
$lnq_e = lnK_F + 1/nlnC_e$	$K_F (L\ mg^{-1})$	0.0010
Plot: lnq_e vs lnC_e	R^2	0.9597
	X^2	0.5987
Temkin	B_1	250.660
$q_e = B_1 lnK_T + B_1 lnC_e$	$K_T (L\ mg^{-1})$	17.0691
Plot: q_e vs. lnC_e	R^2	0.9024
	X^2	0.8632
Dubinin-Radushkevich	q_s	2050.01
$lnq_e = lnq_s - k\varepsilon^2$	$k \times 10^{+6} (mol^2\ kJ^{-2})$	90.000
Plot: lnq_e vs. ε^2	$E (1/2k^{0.5}) (kJ\ mol^{-1})$	0.0745
	R^2	0.9068
	X^2	0.8706

parental generation solutions are then participated to form higher quality individuals from fitness point of view. This iterative process is generally terminates when algorithm reaches to the satisfactory fitness level (Table 3) as detailed elsewhere (Ghaedi et al., 2016a, b).

Table 5
Kinetic parameters for I_2 adsorption (initial I_2 concentration = 250.00 $mg\ L^{-1}$, adsorbent dose = 12.00 mg, Temperature = 47.00 °C, contact time intervals = 0.50–35.00 min).

Model	Parameters	Value of parameters
pseudo -first-order	$k_1(min)$	0.0332
$\ln[q_e - q(t)] = lnq_e - k_1t$	$q_e(mg\ g^{-1})$	981.12
plot: $\ln[q_e - q(t)]$ Vs t	R^2	0.9613
pseudo -second-order	$k_2(min)$	1.05×10^{-4}
$\frac{t}{q(t)} = \frac{t}{q_e} + \frac{1}{k_2q_e^2}$	$q_e(mg\ g^{-1})$	1800.70
	R^2	0.9982
Plot: $t/(q(t))$ vs t		
intraparticle diffusion	$K_{diff}(mg\ g^{-1}\ min^{-1/2})$	0.0981
$q_t = k_{id}t^{\frac{1}{2}} + C$	R^2	0.6825
Plot: q_t vs. $t^{\frac{1}{2}}$	$C(mg\ g^{-1})$	1200.20
Elovich model	$\beta(g\ mg^{-1})$	8.33×10^{-3}
$q_t = \frac{1}{\beta}ln\alpha\beta + \frac{1}{\beta}lnt$	$\alpha(mg\ g^{-1}min^{-1})$	1129.74
Plot: q_t vs. lnt	R^2	0.7215

2.8. Equilibrium and models

Equilibrium data was used to describe the mechanism of I_2 adsorption on **Mg − Co − Al − LDH − g − C_3N_4 − NC**. Isotherm and kinetic studies were conducted at different initial concentration of I_2 (50.00 − 250 mg/L) and time intervals (0.50–35.00 min), respectively. Except for the mentioned parameters, the experimental procedure in this section was similar to that described in section 2.4. Moreover, the adsorption capacity (q_t, mg/g) of the **Mg − Co − Al − LDH − g − C_3N_4 − NC** was estimated using Eq. 3. The corresponding results were employed into the different kinetic and isotherm models as listed in Tables 4 and 5.

$$q_e = \frac{(C_f - C_i)V}{W} \tag{3}$$

Where C_i, C_f defined before. V implies on the volume of I_2-containing aqueous (L), and W refers the adsorbent dose (g).

3. Result and discussion

3.1. Characterization

Fig. 2 represent the Field emission SEM (FESEM) images of $g − C_3N_4$, Mg− Co− Al− LDH, and Mg− Co− Al− LDH− $g − C_3N_4$ samples. Fig. 2a–b displays that the Mg− Co− Al− LDH particles are lotus leaf like in shape and uniform in size most almost at a nanometer scale. Also, Fig. 2c–d indicate a graphite-created irregular two-dimensional layered structure that, mainly made up of a few randomly folded thin sheets. In the Mg− Co− Al− LDH− $g − C_3N_4$ − NC (i.e. Fig. 2e–f),
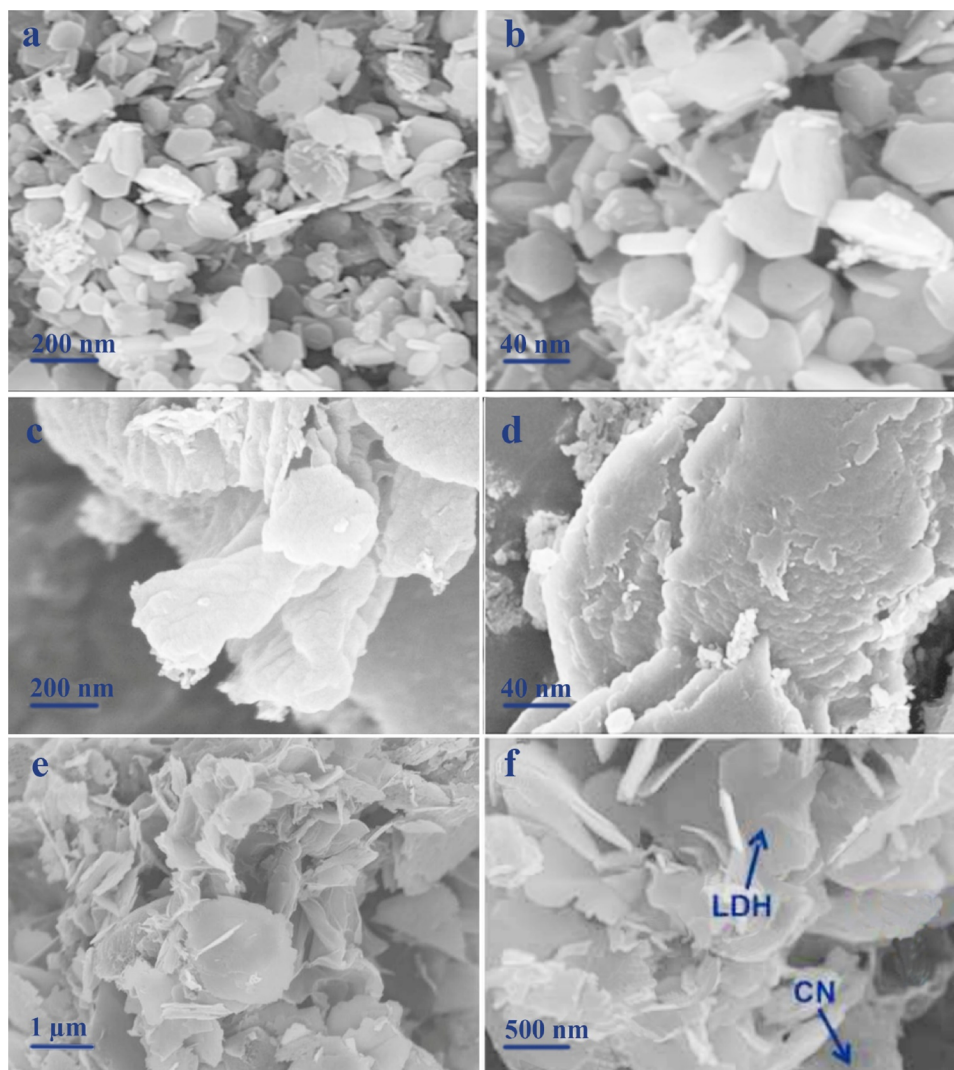

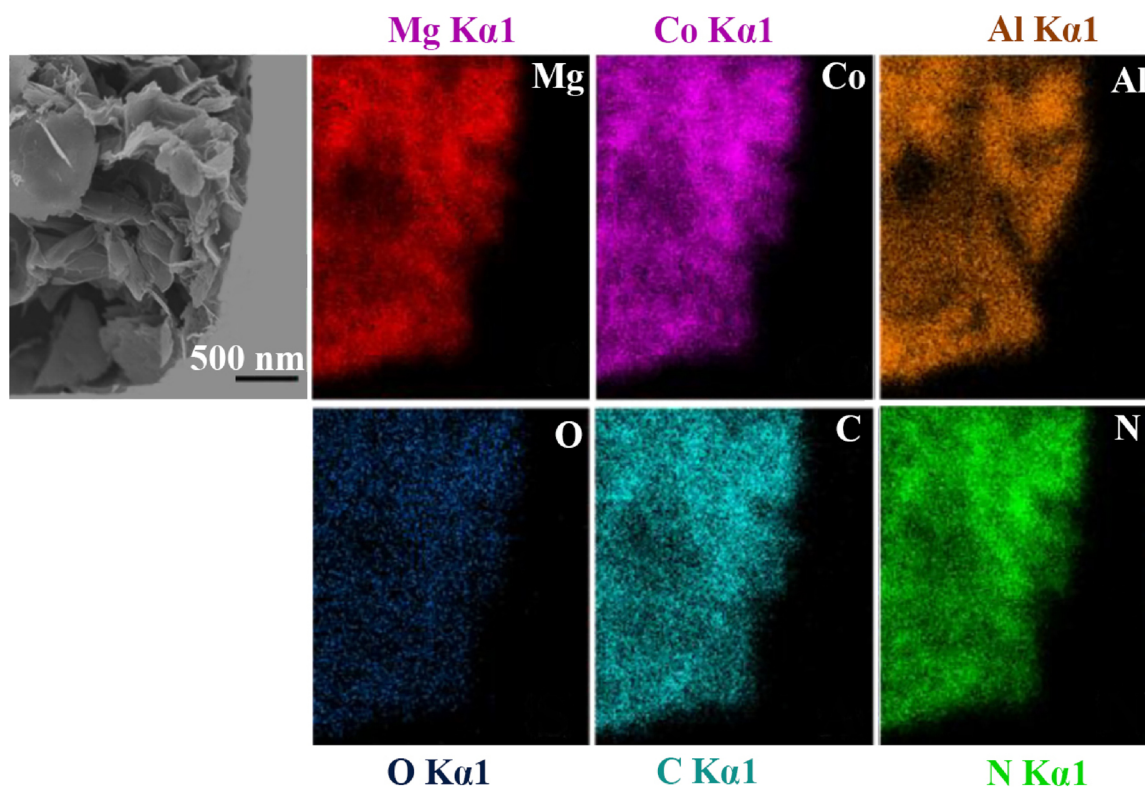**Fig. 2.** SEM image of Mg-Co-Al-LDH (a–b), g-C₃N₄ (b–c) and Mg-Co-Al-LDH @g-C₃N₄-NC (e–f).

Fig. 3. XRD pattern of g-C₃N₄, Mg-Co-Al-LDH, and Mg-Co-Al-LDH @g-C₃N₄-NC.

Table 6
The composition and the elements present at the LDH and LDH@ g-C₃N₄ nanocomposite samples as determined by The EDS.

sample	EDX method		
	Mg	Co	Al
LDH	20.20	14.95	9.85
LDH@ g-C₃N₄	3.00	1.90	0.95

the surface of the Mg− Co− Al− LDH are uniformly entrapped into $g - C_3N_4$, demonstrating a interaction between LDH and $g - C_3N_4$ through either charge transfer or electrostatic interactions (Nayak et al., 2015).

Furthermore, Electron Dispersive Spectra (EDS) elemental mapping images (Fig. 3) confirm the presence all constituents of Mg, Co, Al, C, N, and O at the synthesized nanocomposite. A similar distribution of the elements in the LDH@ $g - C_3N_4$ mapping pattern obviously reveals that both LDH and g-C₃N₄ phases are completely mixed and closely incorporated each other. Furthermore, the chemical compositions of both LDH and $Mg - Co - Al - LDH@g - C_3N_4$ were determined by EDX analysis and summarized in Table 6.

A detailed morphology of $Mg - Co - Al - LDH@g - C_3N_4 - NC$ was further studied using TEM images (Fig. 4a–d). The micrograph TEM of g-C₃N₄ (i.e. Fig. 4(a) and (b)) shows a typical irregular 2D layered structure, which is in close agreement with obtained results using SEM images (Fig. 2(c–d)). The observed leaf like structure at $Mg - Co - Al - LDH$ disappeared at $Mg - Co - Al - LDH@g - C_3N_4 - NC$. Whereas, the ultrathin 2D LDH sheets morphology can be observed on the surface of $g - C_3N_4$ (Fig. 4c–d), may be due to occurring a successful self-assembly by electrostatic interactions between of $g - C_3N_4$ and $Mg - Co - Al - LDH$. However, TEM image clearly shows a interaction between $g - C_3N_4$ and $Mg - Co - Al - LDH$ due to their different surface charges.

The XRD patterns of Mg− Co− Al− LDH, $g - C_3N_4$, and $Mg - Co - Al - LDH - g - C_3N_4 - NC$ are given in Fig. 5. In XRD pattern of $g - C_3N_4$ two characteristic peaks at 13° and 27.5° are observed which are corresponding to the in-plane (100) and interlayered stacking pattern (002), respectively (JCPDS data: 87–1526). The diffraction peaks of Mg− Co− Al− LDH− $g - C_3N_4 - NC$ (Fig. 5) seems similar to that of Mg− Co− Al− LDH and $g - C_3N_4$, but in a weaker intensity. The XRD diagram of Mg− Co− Al− LDH shows a rhombohedral shape with characteristic (003), (006), (009), (015), (018), (110), and (113) diffraction peaks. Moreover, no diffraction peaks of CO₂O₃ were observed in the XRD pattern may be due to completely doping of Co in the LDH lattice. By comparison XRD patterns, it can be stated that the diffraction peaks of the Mg− Co− Al− LDH− $g - C_3N_4 - NC$ patterns were really matched with those of Mg− Co− Al− LDH and $g - C_3N_4$ samples, indicating a successful incorporation of Mg− Co− Al− LDH into the $g - C_3N_4$ structure.

FTIR spectroscopy is a valuable tool for the description of LDH that it is relating the vibrations in the rhombohedral lattice, the interlayer anions, and the hydroxyl groups. The FTIR spectra for Mg− Co− Al− LDH and $g - C_3N_4$ nanosheet in the region 400–4000 cm^{-1} are illustrated in Fig. 6. The broad band at $3000 - 3500$ cm⁻¹ in g-C₃N₄ is assigned to the stretching vibrational modes of –NH₂- and –NH– groups (Fig. 6). Stretching vibrations of the nitrogen containing heterocycles were observed at $1100 - 1700$ cm⁻¹. Moreover, the band at 810 cm⁻¹ is related to the bending of triazine or heptazine units (Liu et al., 2019). The vibration and bending mode of CO_3^{2-} were appeared at 1400 cm⁻¹ in the spectra of LDH and $LDH@g - C_3N_4$ samples that may be considered as entrapped anions in the interlayer.

Based on previous reports, the observed peaks positioned at 400 to 800 cm⁻¹ can be considered as stretching mode for metal–oxygen (M−O) (Saito et al., 2018). The band around 1050 cm⁻¹ shows out-of-plane vibrations mode deformation of Al−OH. Besides, the stretching and bending vibrations located at 3450 and 2500 cm⁻¹ can be assigned to hydrogen bonding between the water molecules and hydroxide OH groups of LDH. The water bend band was detected at 1610 cm⁻¹. The FTIR spectra of synthesized nanocomposite confirms that all vibrational
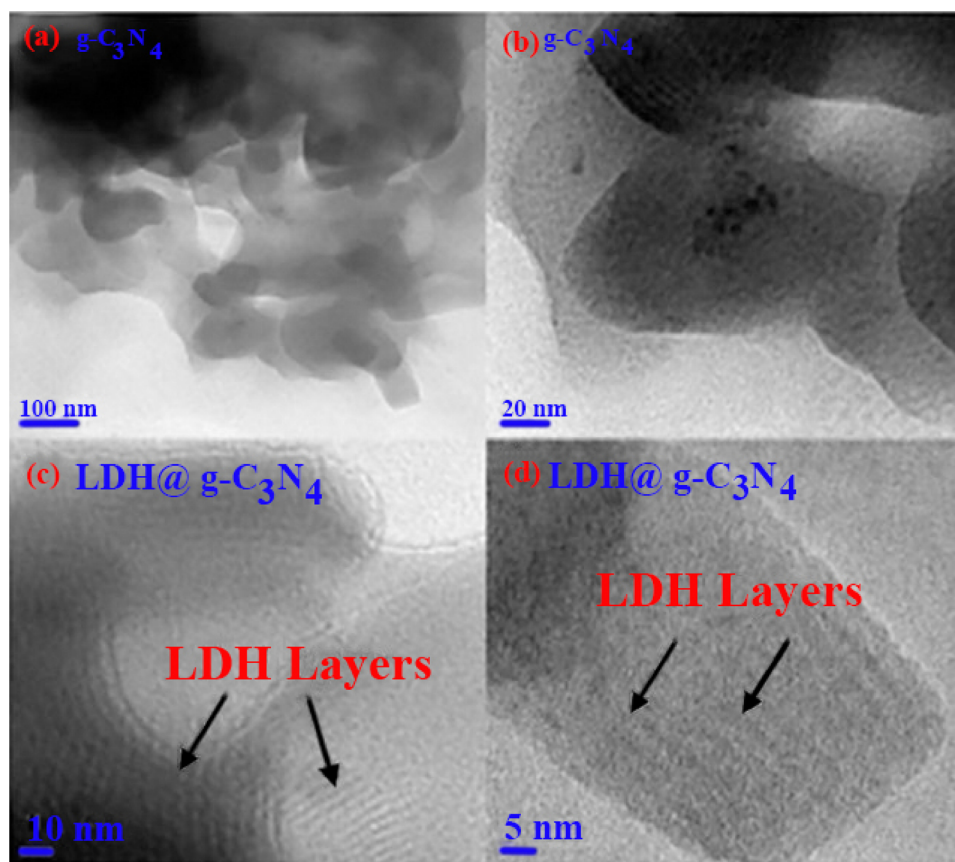
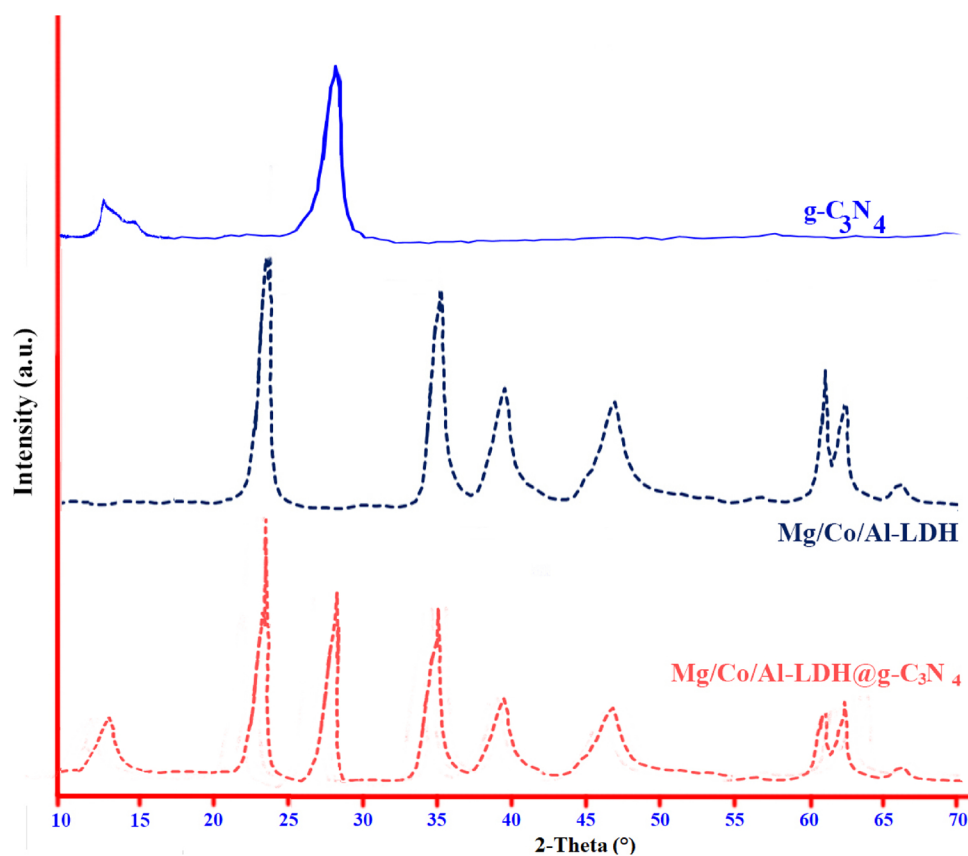**Fig. 4.** FTIR spectra: g-C$_3$N$_4$, Mg-Co-Al-LDH and Mg-Co-Al-LDH@ g-C$_3$N$_4$.

Fig. 5. EDS spectrum and corresponding elemental mapping images of Mg-Co-Al-LDH@g-C$_3$N$_4$-NC.
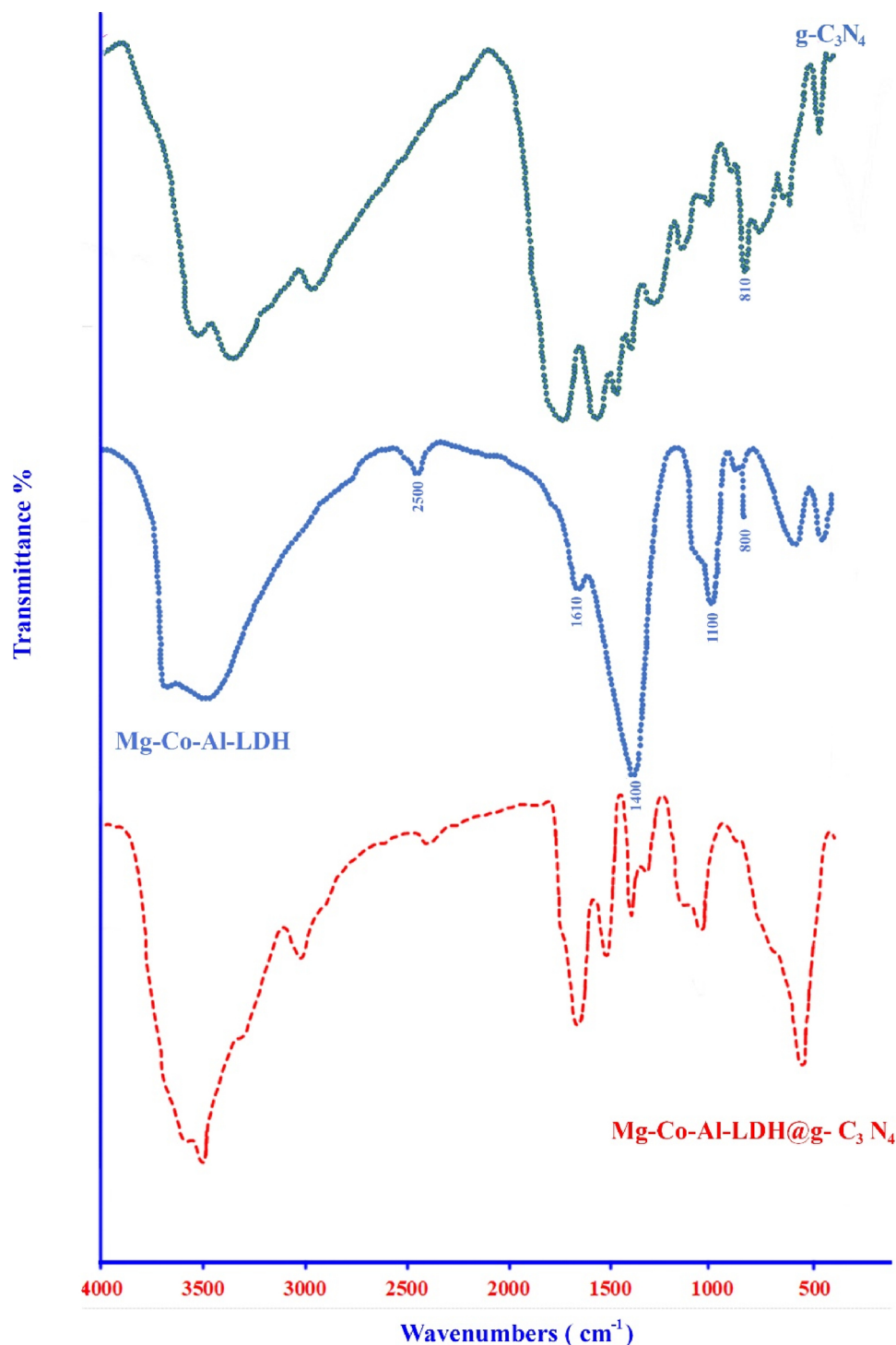
Fig. 6. TEM images of as-prepared g-C₃N₄ (a–b) and Mg-Co-Al-LDH@ g-C₃N₄ (c–d) samples.

Table 7
The specific surface area and structural properties of synthesized Mg-Co-Al-LDH, g-C₃N₄ and Mg-Co-Al@ g-C₃N₄-NC.

nanoadsorbent	BET $(m^2 . g^{-1})$	Total pore volume $(cm^3 . g^{-1})$	Average Pore size (nm)
g-C₃N₄	139.40	0.320	29.32
Mg-Co-Al-LDH	21.90	0.590	13.59
Mg-Co-Al@g-C₃N₄-NC	170.95	0.620	27.90

modes of LDH are appeared in graphite carbon nitride@ Mg-Co-Al-LDH nanocomposite samples indicating the successfully grown of LDH on $g - C_3N_4$ nanosheets.

Nitrogen adsorption/desorption analyses reveal the specific surface area (SSA) and the average pore size of the samples under Brunauer–Emmett–Teller (BET) and Barrett–Joyner–Halenda (BJH) techniques, respectively (Li et al., 2013). The textual analysis by BET showed a type of IV isotherms for both $Mg - Co - Al - LDH$ and $LDH@g - C_3N_4$ nanocomposite, which implies on a mesoporous-type structure. Based on the BET surface area analyses, the total specific surface area (SSA) for LDH, g-C₃N₄, and $Mg - Co - Al - LDH@g - C_3N_4 - NC$ was found to
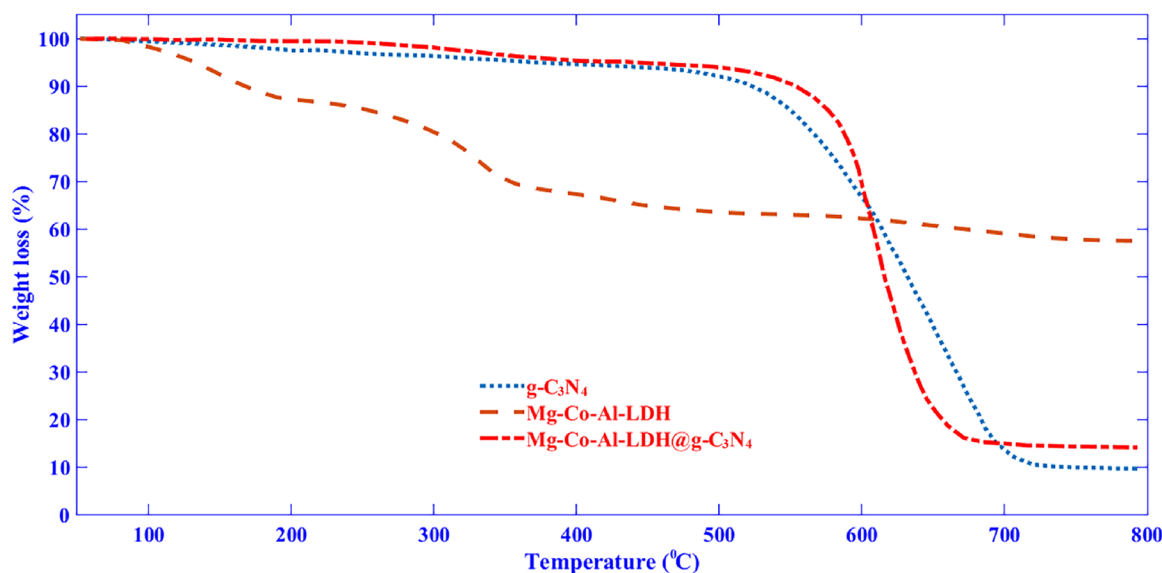
Fig. 7. TGA curves of the Mg-Co-Al-LDH, g-C$_3$N$_4$, Mg-Co-Al-LDH@g-C$_3$N$_4$ samples.
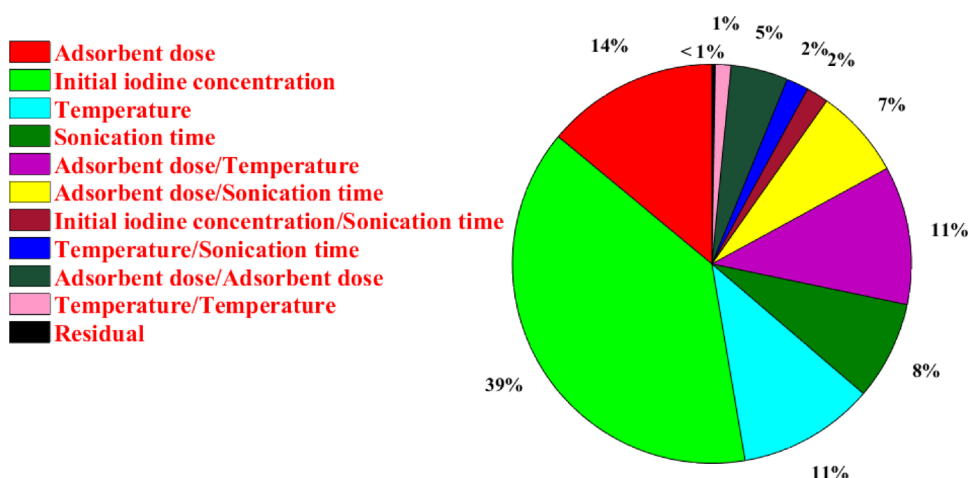

Fig. 8. Sources of variability in removal of I_2.

be 21, 139, and 170 m^2 g^{-1}, respectively (Table 7), all with a pore size < 30 Å. Owning to the best surface characteristics i.e. the highest SSA and pore volume, the $Mg - Co - Al - LDH@g - C_3N_4 - NC$ can be considered as an appropriate adsorbent for removal of different pollutants.

TGA measurements were conducted to investigate the amount of LDH in the prepared $Mg - Co - Al - LDH@g - C_3N_4 - NC$ under N$_2$ environment at a 10 °C min^{-1} heating rate. For the bare $Mg - Co - Al - LDH$ two regions were observed in below 200 °C and at the 250–350 °C range, respectively (Fig. 7) (Sha et al., 2019). The first weight loss is contributed to the vaporization of interlayer and surface - adsorbed water molecules. The second can be due to de-hydroxylation of the brucite-like layers and the degradation of the carbonates and/or nitrate anions in the interlayer (Zhong et al., 2019). Besides, $g - C_3N_4$ decomposition happened at 500 °C and finished at ~750 °C can be ascribed to the combustion of g-C$_3$N$_4$.

The TGA of the $LDH@g - C_3N_4$ nanocomposite showed a similar trend to what was seen in bare $Mg - Co - Al - LDH$ and $g - C_3N_4$ component, although with a poor loss over low temperature regions. However, due to in-situ synthesis, the water molecules and nitrate

anions in the interlayer of $LDH@g - C_3N_4 - NC$ were found very low. Nonetheless, the content of $Mg - Co - Al - LDH$ in the nanocomposite can be calculated based on percentage remainder of $LDH@g - C_3N_4 - NC$ after heating to 800 °C. Consequently, the weight percentages of $Mg - Co - Al - LDH$ in the nanocomposite was found to be ~ 6 % that is in agreement with the results of EDS analysis.

3.2. Models fitting and the related analyses

3.2.1. CCD

Removal of I$_2$ was statistically analyzed using CCD by contributing four critical parameters i.e. adsorbent dose (X_1, $1 - 13$ mg), initial I$_2$ concentration (X_2, $50 - 250$ mg/L), tempreature (X_3, $30 - 50$ °C), and time (X_4, $15 - 35$ min). A total 30 runs with different combinations of these four chosen factors were generated and performed as given in Table 1. Both main and interaction effects of the factors contributed were deduced by ANOVA, regression coefficient, F- and P-values of variables. The developed quadratic model based on ANOVA for I$_2$ capture by the nanocomposite is shown in Eq. 17.

$$I_2 \text{adsorption}(\%) = +217.96 - 11.28 \times X_1 + 0.283 \times X_2 + 6.84 \times X_3 + 10.81 \times X_4 + 0.343 \times X_1 \times X_3 -$$
$$0.276 \times X_1 \times X_4 - 0.0082 \times X_2 \times X_4 + 0.083 \times X_3 \times X_4 + 0.280 \times X_1^2 \tag{4}$$
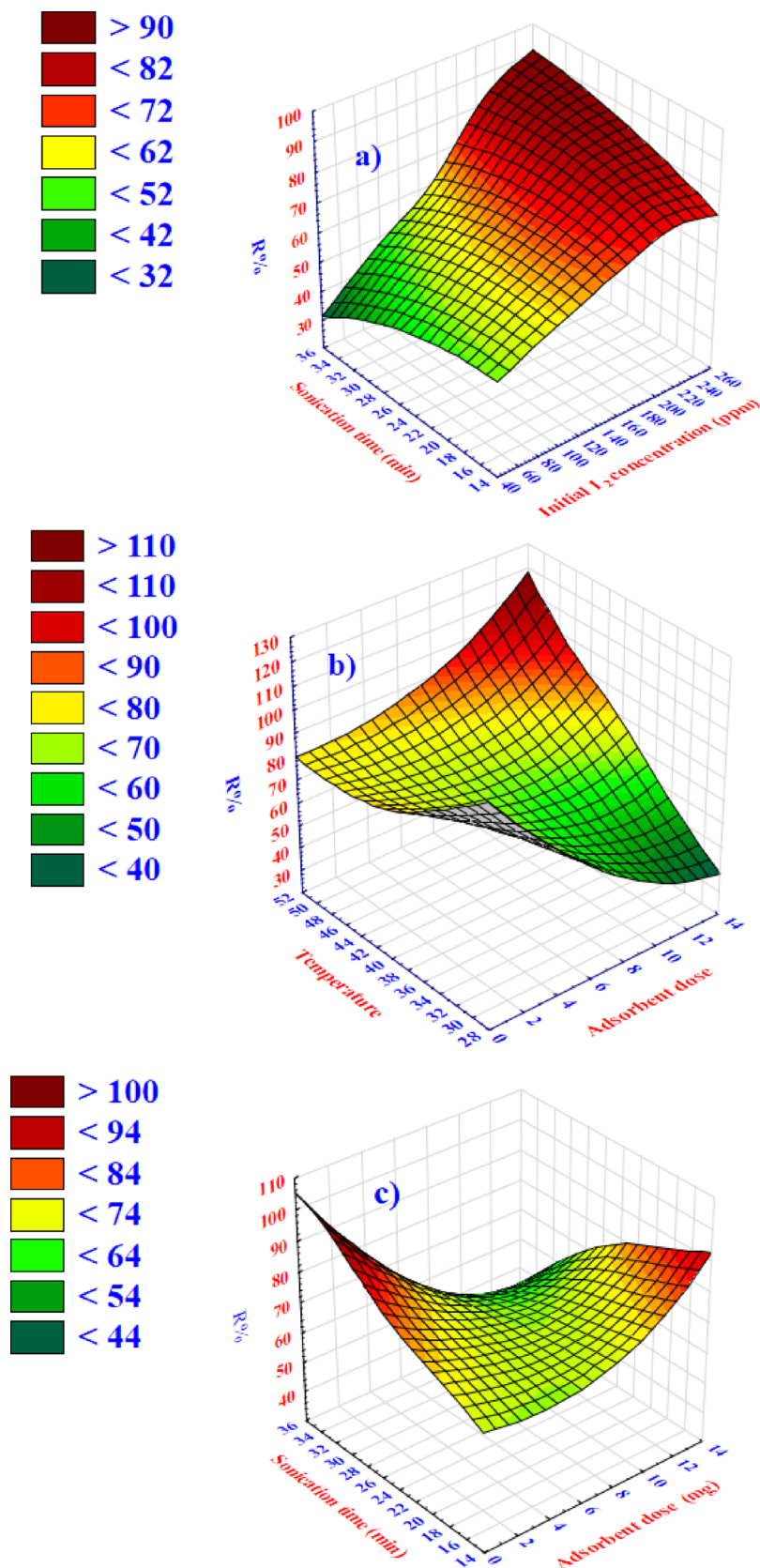
Fig. 9. Response surface plots showing effects of variables: a) I_2 concentration-sonication time, b) adsorbent dose – temperature, c) adsorbent dose - sonication time.

where the algebraic signs indicate the quality of terms' effect on I_2 removal (i.e. either positive or negative effect). The relative importance of the terms as I_2 removal was calculated from ANOVA's sum of square (SS) (Fig. 8). In fact, effect of a parameter on the responses is more significant at higher SS. The degree of the SS in the Fig. 8 clearly implies that the variables significantly effects on I_2 removal by the nano composite as following order: initial I_2 concentration > adsorbent dose > temperature > sonication time.
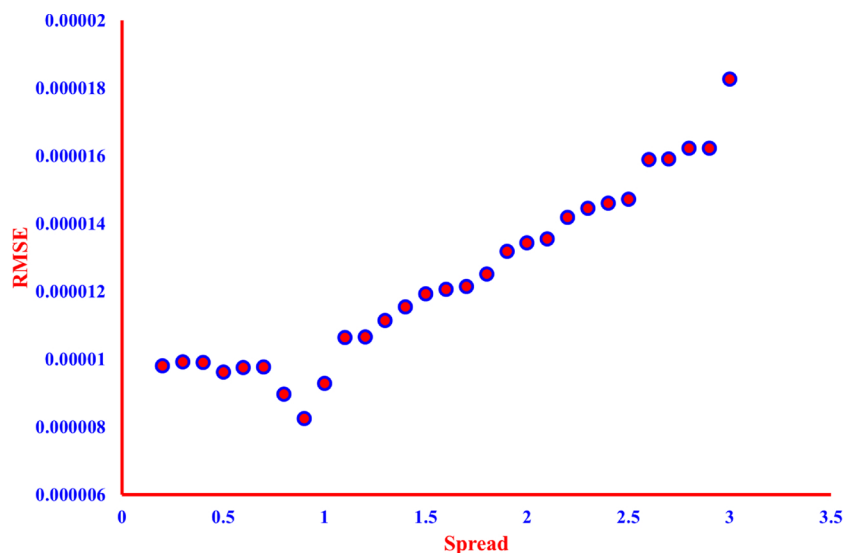
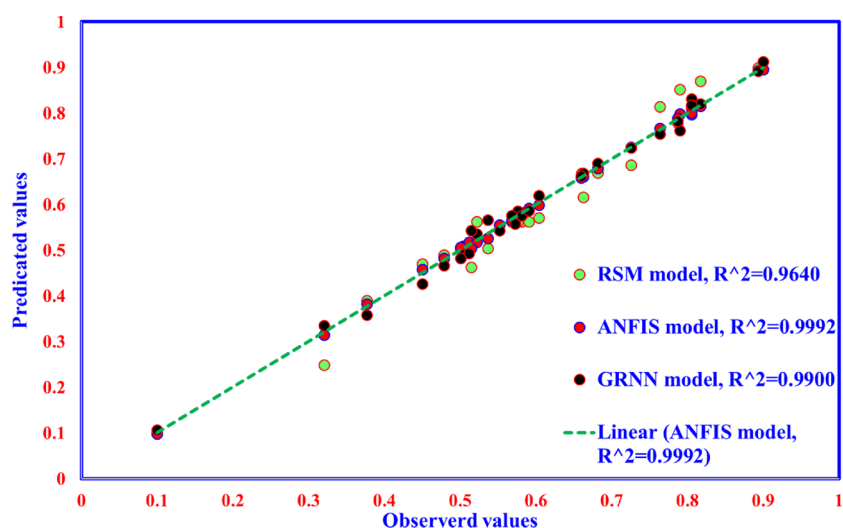**Fig. 10.** The RMSE-spread constant graph for I_2 by GRNN model (GRNN run with training data set).

Fig. 11. The scatter plot of RSM, ANFIS, and GRNN model predicted values versus actual values for I_2.

3.2.1.1. Effect of parameters on I_2 removal by $Mg - Co - Al - LDH@g - C_3N_4 - NC$. The relationship between variables studied as the response was also visualized by 3D surfaces diagrams (Fig. 9). As seen from Fig. 9a, the removal efficiency strongly depends on the I_2 initial concentration, so that this parameter found to be the most effective one on I_2 adsorption by $g - Co - Al - LDH@g - C_3N_4 - NC$ with a relative proportion of $\cong$ 39 % (Fig. 8). This can be ascribed to the simply formation of inner charge complex (adsorbent$^+$I$^-$) in the high concentration.

pH of the solution causes different charges on I_2 surfaces sites. At pH = 7, for example, these molecules mainly exist as iodine and I_3^- form that impose a yellowish-brown color. On the other hand, the nitrogen atom (in the C_3N_4) acts as a base (Lewis) and can create a natural strong interaction with iodine molecule. The adsorption of I_2 molecule on the C_3N_4 occurs through charge transferring from nonbonding orbital of nitrogen to antibonding molecular orbital of iodine molecule (Harijan et al., 2018). Zou et al. reported that in this situation, at first an outer charge complex ($C_3N_4 - I_2$) forms, which in turn undergo an inside transition an finally inner charge complex ($C_3N_4^+I^-$) can be formed. Consequently, the inner charge complex takes up more I_2 and created polyiodide complex (i.e. $C_3N_4^+I_3^-$, $C_3N_4^+I_5^-$ and $C_3N_4^+I_7^-$) (Zou et al., 2017) On the other hand, there are various oxygen-containing functional groups on the $Mg - Co - Al - LDH$ surface which can form

strong bonding with I_2 via charge transfer (Zou et al., 2017) and increase the removal efficiency. Hence, the observed increase in the removal may be explained. In addition, in the $Mg - Co - Al - LDH@g - C_3N_4$ with various nitrogen/oxygen-containing functional groups may be able to forms stronger chemical bonds with I_2 or other ($C_3N_4^+I^-$) complexes can lead to molecular iodine adsorption.

The relationship between adsorbent dose and temperature on the R % plotted on the Fig. 9b. Fig. 9b shows that the I_2 removal improves with increasing adsorbent dose as well as temperature. However, the effect is more pronounced only at the higher dosages (i.e. dose > 8 mg). Meantime, the Sources of variability showed the adsorbent dose has a significant impact on the removal relative to temperature (Fig. 8). But it can be seen (Fig. 9b) that in the low adsorbent dose, the increase of temperature from $30-50\,°C$ has not influence on the removal. But, in the high amount of adsorbent (13 mg) the impact of temperature clearly visible. From eq. 4, it can be deduced that the adsorbent dose has a negative effect on the removal. This phenomenon can be explained by the relationship between adsorbent dose and sonication time (Fig. 9c). Fig. 9c displays the interaction effect between sonication time and adsorbent dose for the adsorption iodine.

As evident in Fig. 9c, in the low sonication time (15 min) and high adsorbent dose, removal efficiency is > 80 %. However, it dropped into
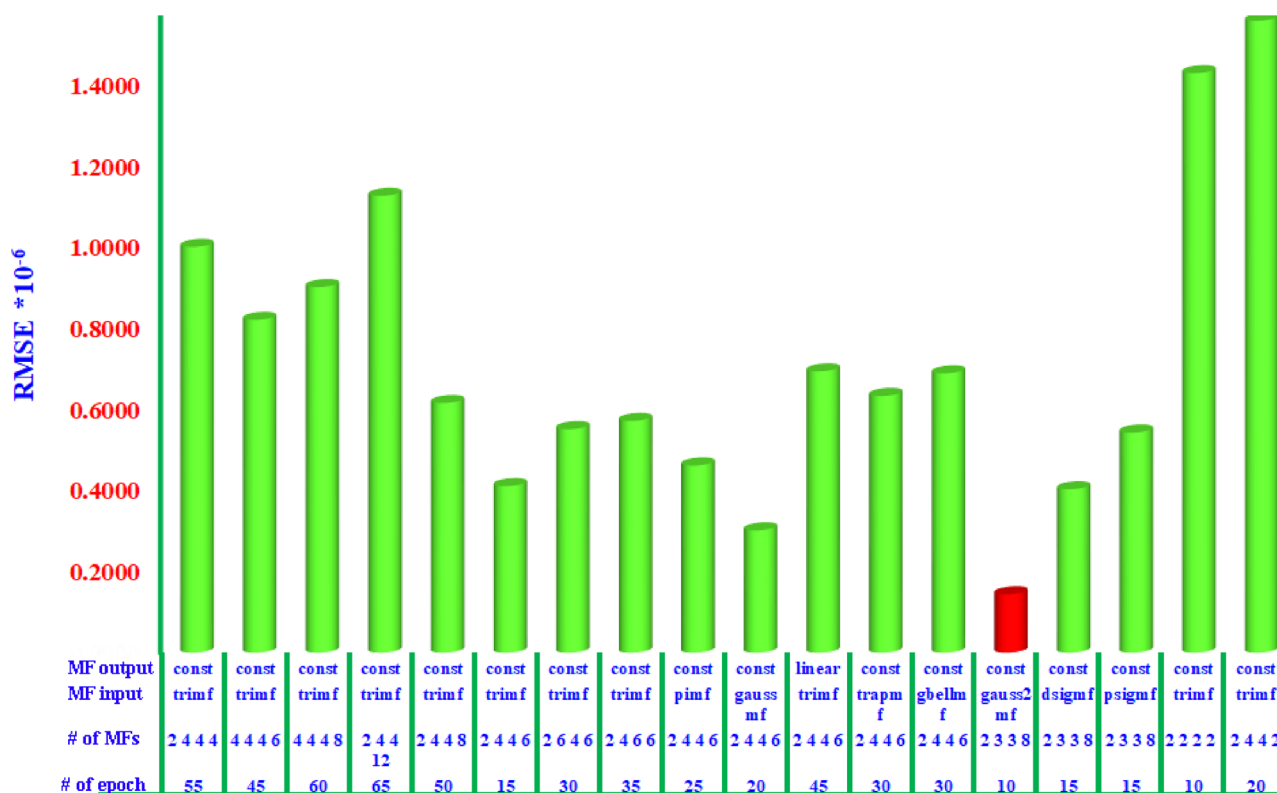
Fig. 12. The RMSE of different ANFIS models (plotted by training set).

MF output	const	const	const	const	const	const	const	const	const	const	linear	const	const	const	const	const	const	const
MF input	trimf	trimf	trimf	trimf	trimf	trimf	trimf	trimf	pimf	gauss mf	trimf	trapmf	gbellmf	gauss2 mf	dsigmf	psigmf	trimf	trimf
# of MFs	2 4 4 4	4 4 4 6	4 4 4 8	2 4 4 12	2 4 4 8	2 4 4 6	2 6 4 6	2 4 6 6	2 4 4 6	2 4 4 6	2 4 4 6	2 4 4 6	2 4 4 6	2 3 3 8	2 3 3 8	2 3 3 8	2 2 2 2	2 4 4 2
# of epoch	55	45	60	65	50	15	30	35	25	20	45	30	30	10	15	15	10	20

the lowest percentage (i.e. < 30 %) at the high sonication time and adsorbent dose. Therefore, as can be seen from Figs. 8 and 9c, sonication time is another effective factor on the adsorption with a relative proportion of 10 %. Moreover, the removal efficiency greatly increased with increasing sonication time in both low nanoadsorbent dose (Fig. 9b) and at high I_2 concentration (Fig. 9a). As, a maxima adsorption observed in the sonication of 36 min and I_2 concentration of 250 ppm (Fig. 9a) and sonication of 36 min and nanoadsorbent of 4 mg (Fig. 9c). Sonication has been extensively reported for the enhanced elimination of contaminates from (waste)water media in recent years. The sonication can extend the adsorbent surface and enhance the mass transfer by the cavitation process (Dil et al., 2017).

For this study, however, we believe that, at low adsorbent dose, the sonication improves the construction of the inner charge complex on the nanoadsorbent via the mass transfer by different mechanisms. But at the high adsorbent dose, sonication may be resulted in the instability of the inner charge complex.

3.2.2. GRNN

The relationship between the variables was also assessed by GRNN model. This meta-modeling approach holds a great capability in non-linear estimation with an easy approximation and quick learning in comparison with other neural networks-based strategies (Lotfinejad et al., 2018). The smooth parameter (also known as spread factor, σ) that plays a critical role in development of a stable ANN model, however, should be selected empirically. In this study, therefore, different values ranged from 0.01–3.0 were assigned for σ and the optimum was considered according to the minimum RMSE in the validation period. Fig. 10 presents the RMSE achieved for different σ values for training set. By assigning 0.9 to σ, the performance of the model for I_2 adsorption reached to its lowest value (i.e. 8.24×10^{-6}). Fig. 11 also shows a high correlation between the anticipated removal efficiencies using the GRNN model against the obtained values.

3.2.3. ANFIS

The selection of optimum structure is the main challenging issue in ANFIS training which is achieved by checking different categories of MFs on input parameters. For this, various ANFIS structures based on hybrid optimization strategy were assessed. In fact, to attain the most accurate model, 21 trials and their own responses as training dataset were involved in 16 different models in terms of eight input MFs along with two output MFs. The epochs' number is another ANFIS network parameter, whose optimal value was determined by the corresponding minimum RMSE. The ANFIS optimization process as types of input and output MF along with number of MFs and epochs is presented in Fig. 12. As presented in Fig. 12, gauss2mf displayed the minimum RMSE (1.437×10^{-6}) with rule and epoch numbers of 192 and 10, respectively. MF structure, input, and output of the model specified to be 2-4-4-6, gauss2mf, and constant, respectively.

A highest coefficient determination ($R^2 = 0.9998$) and lowest RMSE indicated that ANFIS model would be reliable (Fig. 11). Besides, the interactions between all factors contributed were investigated as ANFIS-3D plots, which in the percent of I_2 removal is checked by interaction nano composite dose with I_2 concentration Fig. 13(a), interaction nano composite dose with temperature Fig. 13(b) and interaction nano composite dose with sonication time Fig. 13 (c). Such plots present supportive interpretation on interaction between variables to handle the process appropriately.

As shown in Fig. 13a, the removal efficiency (%) is expected to improve with increase in adsorbent dosages. It can be understood from this figure that the R (%) is maxima particularly in higher initial I_2 concentrations. On the other hand, adsorbent dose showed an insignificant and significant influence on the removal in the low and high initial concentrations of I_2, respectively. It may be this fact that at least a threshold value of iodine in different adsorbent dose is required for removal of I_2. Hence, adsorbent dose showed an insignificant effect in the low iodine concentration. As in the RSM section was stated, at first an outer charge complex ($C_3N_4 - I_2$) between graphite carbon nitride and iodine was formed, and then the inner charge complex in collision
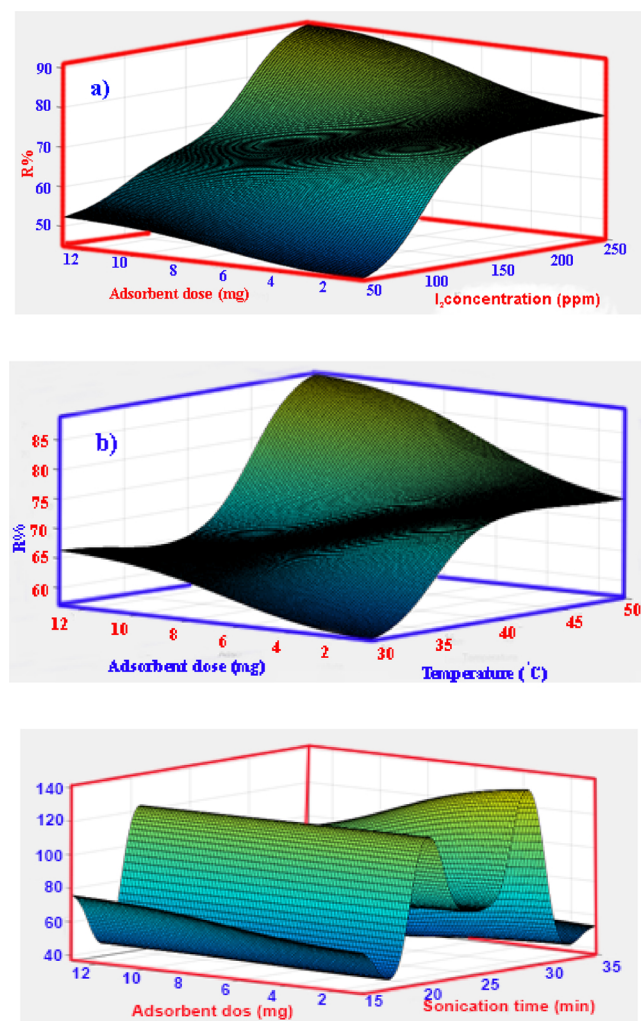
Fig. 13. ANFIS-3D plots showing effects of variables: a) I_2 concentration- nanoadsorbent dose, b) adsorbent dose – temperature, c) adsorbent dose - sonication time.

with more I_2 created polyiodide complex (i.e. $C_3N_4^+I_3^-$, $C_3N_4^+I_5^-$ and $C_3N_4^+I_7^-$). However, in the high adsorbent dose, the outer charge complex ($C_3N_4 - I_2$) is more desirable and extra iodine is needed for creation polyiodide complex. Moreover, this amount of iodine is available. Therefore, at the high iodine concentrations and adsorbent dose the removal efficiency (%) is maxima.

Sonication time (Fig. 13b) seems to be less effected by low and medium initial concentrations. However, sonication time is effective in high concentrations. Moreover, sonication time is more influential than adsorbent dose.

The relationship between adsorbent dose and temperature on the R % predicated by ANFIS plotted on the Fig. 13b. Fig. 13b shows that the I_2 removal improves with increasing adsorbent dose and temperature. As shown, the maximum elimination is attained at high adsorbent dose and temperature. In addition, at the low adsorbent dose, no significant

improvement was observed when the temperature increased at the studied range (Fig. 9b). But, in the high amount of the adsorbent (13 mg) the impact of temperature will be clearly visible.

As evident in Fig. 13c, two distinct maxima can be observed. The first maximum is observed in the low sonication time (15 min) and high or low amount of adsorbent dose. The second maximum is occurred at the high sonication time and low adsorbent dose. However, at both high adsorbent dose and sonication time the removal efficiency falls into the lowest percentage (i.e. < 30 %). Moreover, the removal efficiency greatly increased with increasing sonication time in the low nanoadsorbent dose (Figs. 9c and 13 c). This phenomenon can be explained by this fact that the sonication can extend the surface of the adsorbent material and enhance the mass transfer by the cavitation process. As can be seen from Figs. 9c and 13 c, at the high adsorbent dose, sonication disrupts the inner charge complex and led to a reduction in iodine elimination.

3.3. Comparison of the models' performance

Three models developed i.e. ANFIS, GRNN, and RSM were comprised in terms of the best accuracy to provide maximum reliability in describing the governed behavior in the adsorption process. In fact, accuracy of the models was checked by differences between values predicted by each model and the obtained experimentally. The statistics involved in performance comparison are summarized in Table 8. The statistics were computed from the residuals of normalized values of the obtained and predicted responses. Overall, analyzing all the statistics contributed indicated that the performance order of the models from adequacy, reliability, and generalization point of views is as follow: ANFIS > GRNN > RSM. More details on the statistics role presented in our previous work (Azqhandi et al., 2019).

3.4. Optimization using DF and GA

To find operating conditions in which the "most desirable" response (herein I_2 removal, %) would be achieved, as well as to confirm the accuracy of the introduced model two optimization approaches namely DF and GA were involved. For optimization, $-\alpha$ to $+\alpha$ levels were assigned for the independent factors, whereas higher-the-better criterion was considered for the response. It should be noted that in selection among the runs proposed, high DF value was also considered.

The results suggested that the optimum values to attain a maximum I_2 removal (%) were Mg-Co-Al-LDH@g-C$_3$N$_4$-NC dose 13.00 mg, temperature 50.00 °C, I_2 initial concentration 250.00 mg L^{-1}, and sonication time 35.00 min with DF about 1.00. Fig. 14 presents the graphical DF-derived optimization. Besides, the mentioned values for GA-based optimization were specified to be 12.00 mg, 47.00 °C, 250.00 mg L^{-1}, and 30.00 min, respectively, which in a 95.54 % removal was expected (Table 3). Both GA- and DF- introduced optimum conditions were then confirmed by real validation experiments in triplicate. A high adoption was found between the experimentally achieved and forecasted values particularly in case of GA approach.

3.5. Equilibrium studies

Isotherms data achieved for the adsorption of I_2 onto Mg-Co-Al

Table 8
Comparison of statistical parameters obtained using the ANFIS, GRNN and RSM models.

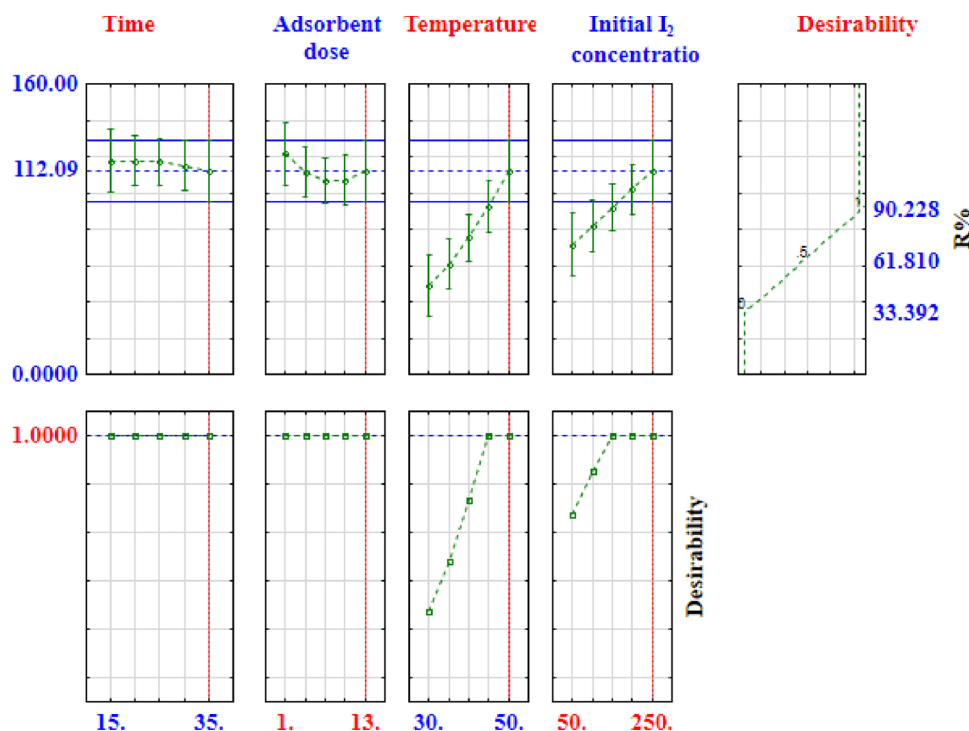| RSM	R^2	SSE	MSE	RMSE	MAE	ARE	AAD	SAE	Hybrid	MPSD	χ^2
	0.9640	0.0270	0.0031	0.0300	0.0223	3.9330	0.9490	0.6678	0.1909	4.6700	0.0496
GRNN	0.9900	< 0.0070	< 0.0008	< 0.0160	0.0126	2.4522	−0.2178	0.3774	0.0487	2.2060	0.0126
ANFIS	greater than 0.999	< 0.0008	< 0.0002	< 0.0051	0.0042	0.8174	0.0726	0.1258	0.0054	0.7353	0.0014

Fig. 14. Profiles for observed, DF and predicated values for the removal of I_2 by Mg-Co-Al -LDH@g-C_3N_4-NC.

Table 9

I_2 adsorption from water on different adsorbents.

Adsorbent	Sorption capacity (mg/g)	pH	Time	Reference
Modified Silica Coated Magnetite Nanoparticles	140.84	7.0-8.0	40 min	(Madrakian et al., 2012)
Activated carbon from different plant-based materials Activated Vinylidene film	− 420-1180 − 650-850	7.00	20 min	(Abe et al., 2001)
Commercial activated carbon Activated Salsola vermiculata plant	272 1178	6.94	20 min	(Bestani et al., 2008)
Fe$_3$O$_4$@PPy	1630	7.00	3h	(Harijan et al., 2018)
Ag-$_{Ag2O}$-CSs	374.91	2.10	120 min	(Yu et al., 2018)
Ag$_2$O-Ag$_2$O$_3$@ZIF-8	232.12	11[a]	30 min	(Chen et al., 2019)
Mg-Co-Al -LDH@g-C$_3$N$_4$-NC	**2200.70**	**7.00**	**30 min**	**This work**

[a] The best performance was achieved at pH = 11, but the authors reported no significant difference in the wide range of.3–11.

-LDH@g-C_3N_4-NC was analyzed by fitting it into different isotherm equations including linear Langmuir, Freundlich, Temkin, and Dubinin–Radushkevich (D–R), whose corresponding R^2 and error analyses (X^2) are summarized in Table 4. It is clear from Table 4 that in comparison with other models, the adsorption of I_2 onto the nanocomposite is better described by using Langmuir isotherm with $R^2 > 0.999$ and $X^2 < 0.500$. The maximum adsorption capacity was specified to be 2200.70 $mg\,g^{-1}$ at pH = 7 and the room temperature. Moreover, the separation factor (R_L) that specifies an adsorption process is favorable when it is lower than one (Igberase et al., 2019), was obtained 0.061-0.142, indicating the desirability of adsorption process. The value of $1/n = 0.8345$ confirmed that the active adsorption sites on the surface of the Mg-Co-Al -LDH@g-C_3N_4-NC were homogeneously distributed, which is desired for interaction with I_2 at the investigated conditions.

The temperature-independent model of D-R forecasts the adsorption energy per unit of adsorbate (E, kJ/mol), along with its maximum adsorption capacity. The former shows the adsorption nature, whose value for the physical adsorption must not be exceed from 8 kJ/mol (Pooralhossini et al., 2018). In this work, the E =0.0745 kJ/mol showed a physical adsorption of I_2 onto Mg-Co-Al-LDH@g-C_3N_4-NC.

3.6. Kinetics of the adsorption

The I_2 molecule adsorption rate onto Mg-Co-Al -LDH@g-C_3N_4-NC was investigated in terms of the different kinetic models, whose corresponding R^2 values are given in Table 5. $R^2 \geq 0.9980$ suggested that I_2 adsorption on the nanocomposite was clearly followed pseudo-second-order kinetic model.

The adsorption capacity of various adsorbents reported in literatures listed in Table 9. It can be seen from Table 9 that the synthesized nanocomposite showed higher adsorption capacity (2200.70 mg/g) in comparison with those reported until now. On the other hand, activated carbon-based adsorbents suffer from cost- and regeneration- related limitations, in addition to facility requirements for their chemical activation. Fortunately, the developed Mg-Co-Al-LDH@g-C_3N_4-NC is a cheap, environmentally friend, and recyclable material. (Dash et al., 2018). Besides, As given in Table 9, at the optimal sonication time (30 min), the capture of iodine by Mg-Co-Al-LDH@g-C_3N_4-NC is higher than that obtained by other studies.

3.7. Regeneration and repeated use

Repeated use capability of an adsorbent is another crucial feature determining economic feasibility in real-scales. Among different
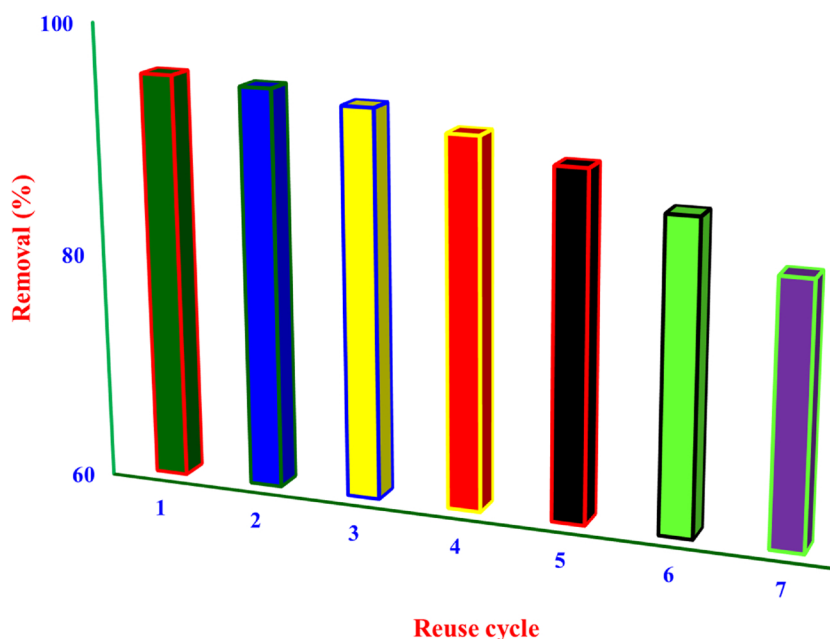
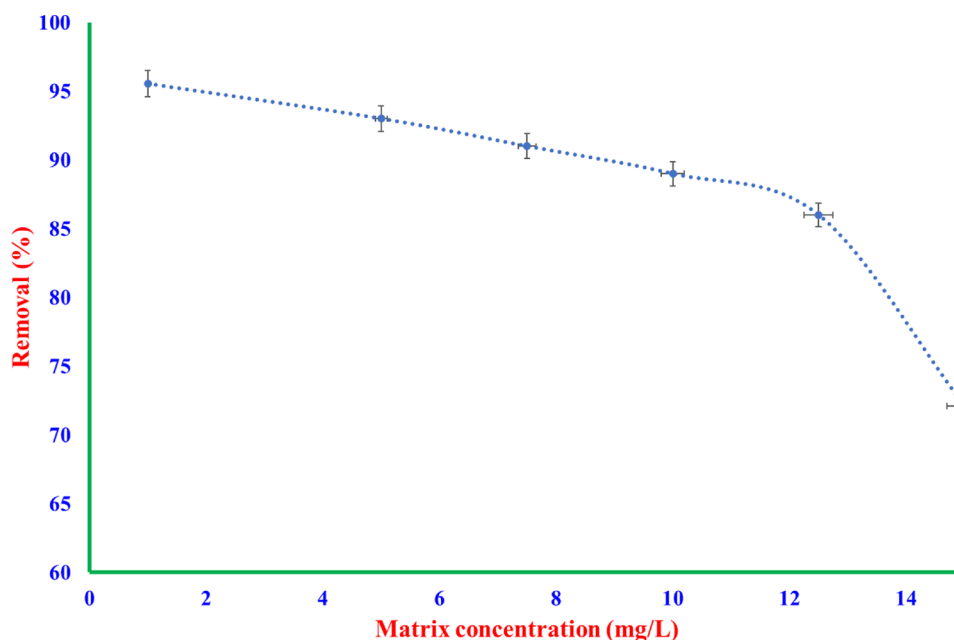**Fig. 15.** Relationship between removal percentage and reuse cycles.

Fig. 16. Interfering ions' effect on I_2 adsorption.

solvents applied for desorption of I_2 molecule form Mg-Co-Al -LDH@g-C_3N_4-NC, ethanol (90%) showed the highest efficiency. The reusability cycles were repeated under the optimal GA-defined conditions (initial I_2 concentration = 250.00 $mg\,L^{-1}$, adsorbent dose = 12.00 mg, Temperature = 47.00 °C, Sonication time = 30.00 min) until no significant losses occurred in the removal efficiency. Fig. 15 illustrates that the Mg-Co-Al -LDH@g-C_3N_4-NC can be reused for seven cycles without breakthrough in the initial removal percentage.

However, as evident in Fig. 15 with recycling of the adsorbent its efficiency dropped to 82.79 % from 95.54 %. A nano adsorbent with loss of about 10 % during four cycles known as a good reusable in real-scales applications (Pooralhossini et al., 2018).

3.8. Thermodynamic of I_2 adsorption

Thermodynamic quantities including Gibbs free energy (ΔG), entropy change (ΔS), and enthalpy change (ΔH) were also determined at a temperature range of 30 − 50 °C. The positive value for ΔH (18.415 kJ/mol) suggested an endothermic nature for the I_2 adsorption on Mg-Co-Al -LDH@g-C_3N_4-NC. The negative ΔG values of −28.661, -29.437, -30.214, −30.990, and −31.767 kJ/mol at 30 °C, 35 °C, 40 °C, 45 °C, and 50 °C, respectively, showed that the process occurred spontaneously from thermodynamic point of view, which supported by the positive value of ΔS (155.289 J/(mol K)) indicating an enhanced randomness at the solid/solution interface throughout the process.

4. Effect of co-exiting ions

Generally, real wastewaters include mixture of cations and anions may competitively occupy available sites on the adsorbent and reduce the removal of the target compound (Nguyen et al., 2013). To examine the effect of Na^+, K^+, Mg^{2+}, Ca^{2+}, Cu^{2+}, Zn^{2+}, Cl^-, CO_3^{2-} and SO_4^{2-} ions on ^{131}I adsorption, six samples were prepared in which the coexisting ions was from 1 to 15 mg/L in 50.0 ml aqueous solution, added to 50 mL of 250 mg/L I_2 and the process was performed at the optimum conditions. The removal of I_2 decreased from 95.54 % to 79.50% when the coexisting concentrations ions increased (Fig. 16) mainly due to the limited active sites on the adsorbent (Nguyen et al., 2013) and the formation of stable complexes (Ghodbane et al., 2008). Nevertheless, the obtained results proposed that I_2 may be successfully captured by Mg-Co-Al -LDH@g-C₃N₄-NC over the various ions in concentration up to 12 mg/L. Moreover, the high selectivity in the removal of I_2 in the presence of competing cations may be due to this fact that the adsorption of I_2 molecule on the C₃N₄ may be occurred through charge transferring from nonbonding orbital of nitrogen to antibonding molecular orbital of iodine molecule (Harijan et al., 2018). Thus, Mg-Co-Al -LDH@g-C₃N₄-NC favourably adsorbed I_2 molecules.

Fig. 16 Interfering ions' effect on I_2 adsorption.

5. Conclusion

In this study, the $g - C_3N_4$ nanocomposite was synthesized first by thermal condensation, functionalized then with $Mg- Co- Al- LDH$ using a hydrothermal method, and utilized as a new adsorbent for iodine sorption from medical-based wastewaters.

The developed $Mg- Co- Al- LDH- g- C_3N_4$ nanoadsorbent was characterized by several techniques which their results can be summarized are as follows: XRD showed a successful incorporation of $Mg- Co- Al- LDH$ into the $g- C_3N_4$ structure with a two-dimensional mesoporous structure. The FE-SEM showed that the surface of the LDHs were uniformly entrapped into the $g- C_3N_4$, indicating a strong interaction between LDH and the $g- C_3N_4$. The FT-IR confirmed the successfully grown of LDH on the surface of the $g- C_3N_4$ nanosheets, whose content was approximated by TGA technique about 6 %, as confirmed further by EDS analysis. The determined total specific surface area by BET test for LDH, $g- C_3N_4$, and $Mg- Co- Al- LDH- g- C_3N_4$ -NC was 21, 139, and 170 m² g⁻¹, respectively, all with a pore size < 30 Å.

The effect of main influential parameters including nanoadsorbent dose, initial iodine concentration, temperature, and sonication time was investigated through three modeling approaches of RSM, GRNN, and ANFIC. Under the GA-introduced optimum conditions a 95.54 % iodine was experimentally removed from the solution in which the values for the above-mentioned factors were set at 13.00 mg, 50.00 °C, 250.00 mg L⁻¹, 35.00 min, respectively. Also, the optimum condition obtained by DF for the above-mentioned factors were 12.00 mg, 47.00 °C, 250.00 mg L⁻¹, 30.00 min, respectively.

Although all models presented appropriate statistics, ANFIS (with MF input of gauss2mf, MF output of constant, rule number of 192, MF structure of 2-4-4-6, and epoch number of 10) showed altogether superior to the others from fitness and estimation capability point of views. All in all, the results of this study showed a very good efficiency for both the LDH integration on nano structure of $g- C_3N_4$ and ANFIS modeling strategy in the removal of radioactive isotope of iodine (i.e. ^{131}I) from aqueous media only in a half-hour which is 1/384 its half-life. Moreover, a highest capacity that has ever been reported (2200.07 mg/g) and recyclability makes this technology can be considered as a potential option in situations where the ^{131}I contamination may occur, e.g. at medical-based treatment sections. Nevertheless, more

studies are still need to overcome the real scale challenges such as the effective separation of the nanocomposite from the media as well as competitive effect of coexisting ions e.g. chloride, sulfate, carbonate, and nitrate.

CRediT authorship contribution statement

Enayatolah Yazdankish: Formal analysis, Funding acquisition, Supervision, Validation, Methodology, Visualization, Investigation, Writing - review & editing. **Maryam Foroughi:** Funding acquisition, Writing - review & editing, Writing - original draft, Software, Validation, Visualization, Investigation. **Mohammad Hossein Ahmadi Azqhandi:** Data curation, Formal analysis, Funding acquisition, Writing - review & editing, Methodology, Project administration, Resources, Supervision, Validation, Visualization, Investigation, Conceptualization.

Declaration of Competing Interest

The authors declare that they have no known competing financial interests or personal relationships that could have appeared to influence the work reported in this paper.

Acknowledgements

References

Abdolmohammad-Zadeh, H., Jouyban, A., Amini, R., 2013. Ultratrace determination of arsenic in water samples by electrothermal atomic absorption spectrometry after preconcentration with Mg–Al–Fe ternary layered double hydroxide nano-sorbent. Talanta 116, 604–610.

Abe, I., Fukuhara, T., Maruyama, J., Tatsumoto, H., Iwasaki, S., 2001. Preparation of carbonaceous adsorbents for removal of chloroform from drinking water. Carbon 39, 1069–1073.

Aghdam, I.N., Varzandeh, M.H.M., Pradhan, B.J.E.E.S., 2016. Landslide Susceptibility Mapping Using an Ensemble Statistical index (Wi) and Adaptive Neuro-Fuzzy Inference System (ANFIS) Model at Alborz Mountains (Iran), vol. 75. pp. 553.

Asfaram, A., Ghaedi, M., Azqhandi, M.A., Goudarzi, A., Dastkhoon, M., 2016. Statistical experimental design, least squares-support vector machine (LS-SVM) and artificial neural network (ANN) methods for modeling the facilitated adsorption of methylene blue dye. RSC Adv. 6, 40502–40516.

Askari, H., Ghaedi, M., Dashtian, K., Azghandi, M.H.A., 2017. Rapid and high-capacity ultrasonic assisted adsorption of ternary toxic anionic dyes onto MOF-5-activated carbon: Artificial neural networks, partial least squares, desirability function and isotherm and kinetic study. Ultrason. Sonochem. 37, 71–82.

Azad, F.N., Ghaedi, M., Dashtian, K., Hajati, S., Pezeshkpour, V., 2016. Ultrasonically assisted hydrothermal synthesis of activated carbon–HKUST-1-MOF hybrid for efficient simultaneous ultrasound-assisted removal of ternary organic dyes and antibacterial investigation: taguchi optimization. Ultrason. Sonochem. 31, 383–393.

Azqhandi, M.A., Shekari, M., 2018. Application of AI in Modeling of Real System in Chemistry.

Azqhandi, M.A., Ghaedi, M., Yousefi, F., Jamshidi, M., 2017. Application of Random forest, Radial basis function neural networks and Central composite design for modeling and/or optimization of the ultrasonic assisted adsorption of brilliant green on ZnS-NP-AC. J. Colloid Interface Sci. 505, 278–292.

Azqhandi, M.H.A., Foroughi, M., Yazdankish, E., 2019. A highly effective, recyclable, and novel host-guest nanocomposite for Triclosan removal: a comprehensive modeling and optimization-based adsorption study. J. Colloid Interface Sci. 551, 195–207.

Bahamonde, S., Díaz-Londoño, G.M., García, M., Albornoz, F., Andrade, P., 2017. Design and implementation of a mobile gamma spectrometry system to in vivo measure the accumulated activity of 131I in patients with thyroid diseases. Appl. Radiat. Isot. 129, 87–95.

Balsley, S.D., Brady, P.V., Krumhansl, J.L., Anderson, H.L., 1996. Iodide retention by metal sulfide surfaces: cinnabar and chalcocite. Environ. Sci. Technol. 30, 3025–3027.

Bestani, B., Benderdouche, N., Benstaali, B., Belhakem, M., Addou, A., 2008. Methylene blue and iodine adsorption onto an activated desert plant. Bioresour. Technol. 99, 8441–8444.

Bingöl, D., Hercan, M., Elevli, S., Kılıç, E., 2012. Comparison of the results of response surface methodology and artificial neural network for the biosorption of lead using black cumin. Bioresour. Technol. 112, 111–115.

Bo, A., Sarina, S., Zheng, Z., Yang, D., Liu, H., Zhu, H., 2013. Removal of radioactive

iodine from water using Ag2O grafted titanate nanolamina as efficient adsorbent. J. Hazard. Mater. 246, 199–205.

Chen, J., Gao, Q., Zhang, X., Liu, Y., Wang, P., Jiao, Y., Yang, Y., 2019. Nanometer mixed-valence silver oxide enhancing adsorption of ZIF-8 for removal of iodide in solution. Sci. Total Environ. 646, 634–644.

Dash, S., Nayak, S., Das, S., Parida, K., 2018. Smart 2D-2D nano-composite adsorbents of LDH-Carbonaceous materials for the removal of aqueous toxic heavy metal ions: a review. Curr. Environ. Eng. 5, 20–34.

Dejaegher, B., Heyden, Y.J.Jop.Vander, 2011. b. Analysis, Experimental designs and their recent advances in set-up, data interpretation, and analytical applications, vol. 56. pp. 141–158.

Dil, E.A., Ghaedi, M., Asfaram, A., 2017. The performance of nanorods material as adsorbent for removal of azo dyes and heavy metal ions: application of ultrasound wave, optimization and modeling. Ultrason. Sonochem. 34, 792–802.

Enayatifar, R., Abdullah, A.H., Isnin, I.F.J.O., Engineering, Li., 2014. Chaos-Based Image Encryption Using a Hybrid Genetic Algorithm and a DNA Sequence, vol. 56. pp. 83–93.

Folens, K., Huysman, S., Van Hulle, S., Du Laing, G.J.S., Technology, P., 2017. Chemical and economic optimization of the coagulation-flocculation process for silver removal and recovery from industrial wastewater. Sep. Purif. Technol. 179, 145–151.

Foroughi, M., Chavoshi, S., Bagheri, M., Yetilmezsoy, K., Samadi, M.T., 2018a. Alum-based sludge (AbS) recycling for turbidity removal in drinking water treatment: an insight into statistical, technical, and health-related standpoints. J. Mater. Cycles Waste Manag. 20, 1999–2017.

Foroughi, M., Rahmani, A.R., Asgari, G., Nematollahi, D., Yetilmezsoy, K., Samarghandi, M.R., 2018b. Optimization of a three-dimensional electrochemical system for tetracycline degradation using box-behnken design. Fresenius Environmental Bulletin 27, 1914–1922.

Gao, X., Li, S., Li, T., Li, G., Ma, H., 2017. gC 3 N 4 as a saturable absorber for the passively Q-switched Nd: LLF laser at 1.3 μm. Photonics Res. 5, 33–36.

Geyikçi, F., Kılıç, E., Çoruh, S., Elevli, S., 2012. Modelling of lead adsorption from industrial sludge leachate on red mud by using RSM and ANN. Chem. Eng. J. 183, 53–59.

Ghaedi, M., Khafri, H.Z., Asfaram, A., Goudarzi, A., 2016a. Response surface methodology approach for optimization of adsorption of Janus green B from aqueous solution onto ZnO/Zn (OH) 2-NP-AC: kinetic and isotherm study. Spectrochim. Acta A. Mol. Biomol. Spectrosc. 152, 233–240.

Ghaedi, M., Azad, F.N., Dashtian, K., Hajati, S., Goudarzi, A., Soylak, M., 2016b. Central composite design and genetic algorithm applied for the optimization of ultrasonic-assisted removal of malachite green by ZnO Nanorod-loaded activated carbon. Spectrochim. Acta A. Mol. Biomol. Spectrosc. 167, 157–164.

Ghodbane, I., Nouri, L., Hamdaoui, O., Chiha, M., 2008. Kinetic and equilibrium study for the sorption of cadmium (II) ions from aqueous phase by eucalyptus bark. J. Hazard. Mater. 152, 148–158.

Harijan, D.K., Chandra, V., Yoon, T., Kim, K.S., 2018. Radioactive iodine capture and storage from water using magnetite nanoparticles encapsulated in polypyrrole. J. Hazard. Mater. 344, 576–584.

Hoskins, J.S., Karanfil, T., Serkiz, S.M., 2002. Removal and sequestration of iodide using silver-impregnated activated carbon. Environ. Sci. Technol. 36, 784–789.

Hu, R., Wen, S., Zeng, Z., Huang, T., 2017. A short-term power load forecasting model based on the generalized regression neural network with decreasing step fruit fly optimization algorithm. Neurocomputing 221, 24–31.

Igberase, E., Ofomaja, A., Osifo, P., 2019. Enhanced heavy metal ions adsorption by 4-aminobenzoic acid grafted on chitosan/epichlorohydrin composite: kinetics, isotherms, thermodynamics and desorption studies. Int. J. Biol. Macromol. 123, 664–676.

Jang, J.-S., 1993. ANFIS: adaptive-network-based fuzzy inference system, IEEE transactions on systems, man. Cybernetics 23, 665–685.

Kaplan, D.I., Serne, R.J., Parker, K.E., Kutnyakov, I.V., 2000. Iodide sorption to subsurface sediments and illitic minerals. Environ. Sci. Technol. 34, 399–405.

Kentjono, L., Liu, J., Chang, W., Irawan, C., 2010. Removal of boron and iodine from optoelectronic wastewater using Mg–Al (NO3) layered double hydroxide. Desalination 262, 280–283.

Khuntia, S.R., Panda, S., 2012. Simulation study for automatic generation control of a multi-area power system by ANFIS approach. Appl. Soft Comput. 12, 333–341.

Kodama, H., 1999. Removal of iodide ion from simulated radioactive liquid waste. Czechoslov. J. Phys. 49, 971–977.

Li, Y., Du, Q., Wang, J., Liu, T., Sun, J., Wang, Y., Wang, Z., Xia, Y., Xia, L., 2013. Defluoridation from aqueous solution by manganese oxide coated graphene oxide. J. Fluor. Chem. 148, 67–73.

Liao, Q., Zou, D., Pan, W., Linghu, W., Shen, R., Li, X., Asiri, A.M., Alamry, K.A., Sheng, G., Zhan, L., 2018. Highly efficient capture of Eu (III), La (III), Nd (III), Th (IV) from aqueous solutions using g-C3N4 nanosheets. J. Mol. Liq. 252, 351–361.

Liu, S., Kang, S., Wang, H., Wang, G., Zhao, H., Cai, W., 2016. Nanosheets-built flowerlike micro/nanostructured Bi2O2. 33 and its highly efficient iodine removal performances. Chem. Eng. J. 289, 219–230.

Liu, X., Jin, A., Jia, Y., Xia, T., Deng, C., Zhu, M., Chen, C., Chen, X., 2017. Synergy of adsorption and visible-light photocatalytic degradation of methylene blue by a bifunctional Z-scheme heterojunction of WO3/g-C3N4. Appl. Surf. Sci. 405, 359–371.

Liu, S., Dong, W., Zeng, X., Guo, Z., Zong, P., Li, B., Meng, X., Zuo, G., 2019. β-cyclodextrin modified g-C3N4 nanosheet: a fluorescent drug carrier with ultrahigh drug loading capacity and pH-responsive release. J. Chem. Technol. Biotechnol. 94, 628–633.

Lotfinejad, M., Hafezi, R., Khanali, M., Hosseini, S., Mehrpooya, M., Shamshirband, S., 2018. A comparative assessment of predicting daily solar radiation using bat neural network (BNN), generalized regression neural network (GRNN), and neuro-fuzzy

(NF) system: a case study. Energies 11, 1188.

Ma, S., Islam, S.M., Shim, Y., Gu, Q., Wang, P., Li, H., Sun, G., Yang, X., Kanatzidis, M.G., 2014. Highly efficient iodine capture by layered double hydroxides intercalated with polysulfides. Chem. Mater. 26, 7114–7123.

Madrakian, T., Afkhami, A., Zolfigol, M.A., Ahmadi, M., Koukabi, N., 2012. Application of modified silica coated magnetite nanoparticles for removal of iodine from water samples. Nano-micro Lett. 4, 57–63.

Montenero, M.P., Dilbone, E.K., Waples, J.T., 2017. Using medically-derived iodine-131 to track sewage effluent in the Laurentian Great Lakes. Water Res. 123, 773–782.

Mostafaei, M., Javadikia, H., Naderloo, L., 2016. Modeling the effects of ultrasound power and reactor dimension on the biodiesel production yield: comparison of prediction abilities between response surface methodology (RSM) and adaptive neuro-fuzzy inference system (ANFIS). Energy 115, 626–636.

Mu, W., Yu, Q., Li, X., Wei, H., Jian, Y., 2017. Niobate nanofibers for simultaneous adsorptive removal of radioactive strontium and iodine from aqueous solution. J. Alloys. Compd. 693, 550–557.

Najafzadeh, M., Etemad-Shahidi, A., Lim, S.Y., 2016. Scour prediction in long contractions using ANFIS and SVM. Ocean. Eng. 111, 128–135.

Nayak, S., Mohapatra, L., Parida, K., 2015. Visible light-driven novel gC 3 N 4/NiFe-LDH composite photocatalyst with enhanced photocatalytic activity towards water oxidation and reduction reaction. J. Mater. Chem. A 3, 18622–18635.

Nguyen, T., Ngo, H., Guo, W., Zhang, J., Liang, S., Yue, Q., Li, Q., Nguyen, T., 2013. Applicability of agricultural waste and by-products for adsorptive removal of heavy metals from wastewater. Bioresour. Technol. 148, 574–585.

Omidi, M.H., Azad, F.N., Ghaedi, M., Asfaram, A., Azqhandi, M.H.A., Tayebi, L., 2017. Synthesis and characterization of Au-NPs supported on carbon nanotubes: application for the ultrasound assisted removal of radioactive UO22+ ions following complexation with Arsenazo III: spectrophotometric detection, optimization, isotherm and kinetic study. J. Colloid Interface Sci. 504, 68–77.

Omidi, M.H., Azqhandi, M.H.A., Ghalami-Choobar, B., 2018. Sonochemistry: a good, fast and clean method to promote the removal of Cu (ii) and Cr (vi) by MWCNT/CoFe 2 O 4@ PEI nanocomposites: optimization study. New J. Chem. 42, 16307–16328.

Osmanlioglu, A.E., 2006. Treatment of radioactive liquid waste by sorption on natural zeolite in Turkey. J. Hazard. Mater. 137, 332–335.

Panda, B.N., Bahubalendruni, M.V.A.R., Biswal, B.B.J.N.C., 2015. Applications, A general regression neural network approach for the evaluation of compressive strength of FDM prototypes. Neural Comput. Appl. 26, 1129–1136.

Pooralhossini, J., Zanjanchi, M.A., Ghaedi, M., Asfaram, A., Azqhandi, M.H.A., 2018. Statistical optimization and modeling approach for azo dye decolorization: combined effects of ultrasound waves and nanomaterial-based adsorbent. Appl. Organomet. Chem. 32 (3), e4205.

Rose, P.S., Swanson, R.L., Cochran, J.K., 2012. Medically-derived 131I in municipal sewage effluent. Water Res. 46, 5663–5671.

Saito, G.P., Romero, J.H.S., Cebim, M.A., Davolos, M.R., 2018. Eu (III) doped LDH intercalated with cinnamate anion as multifunctional sunscreens. J. Lumin. 203, 160–164.

Salehi, G., Abazari, R., Mahjoub, A.R., 2018. Visible-light-Induced graphitic–C3N4@ nickel–Aluminum layered double hydroxide nanocomposites with enhanced photocatalytic activity for removal of dyes in water. Inorg. Chem. 57, 8681–8691.

Samarghandi, M.R., Khiadani, M., Foroughi, M., Nasab, M.J., 2016. Defluoridation of water using activated alumina in presence of natural organic matter via response surface methodology. Environ. Sci. Pollut. Res. - Int. 23, 887–897.

Sanati, S., Rezvani, Z., 2019. g-C3N4 nanosheet@ CoAl-layered double hydroxide composites for electrochemical energy storage in supercapacitors. Chem. Eng. J. 362, 743–757.

Sanchez-Polo, M., Rivera-Utrilla, J., Salhi, E., Von Gunten, U., 2007. Ag-doped carbon aerogels for removing halide ions in water treatment. Water Res. 41, 1031–1037.

Sepehr, M.N., Yetilmezsoy, K., Marofi, S., Zarrabi, M., Ghaffari, H.R., Fingas, M., Foroughi, M., 2014. Synthesis of nanosheet layered double hydroxides at lower pH: optimization of hardness and sulfate removal from drinking water samples. J. Taiwan Inst. Chem. Eng. 45, 2786–2800.

Sha, H., Zhang, Y., Wang, Y., Ke, H., Xiong, X., Jia, N., 2019. Electrochemiluminescence resonance energy transfer biosensor between the glucose functionalized MnO2 and g-C3N4 nanocomposites for ultrasensitive detection of concanavalin A. Biosens. Bioelectron. 124, 59–65.

Tonda, S., Jo, W.-K., 2018. Plasmonic Ag nanoparticles decorated NiAl-layered double hydroxide/graphitic carbon nitride nanocomposites for efficient visible-light-driven photocatalytic removal of aqueous organic pollutants. Catal. Today 315, 213–222.

Warchoł, J., Misaelides, P., Petrus, R., Zamboulis, D., 2006. Preparation and application of organo-modified zeolitic material in the removal of chromates and iodides. J. Hazard. Mater. 137, 1410–1416.

Witek-Krowiak, A., Chojnacka, K., Podstawczyk, D., Dawiec, A., Pokomeda, K., 2014. Application of response surface methodology and artificial neural network methods in modelling and optimization of biosorption process. Bioresour. Technol. 160, 150–160.

Yang, D., Sarina, S., Zhu, H., Liu, H., Zheng, Z., Xie, M., Smith, S.V., Komarneni, S., 2011. Capture of radioactive cesium and iodide ions from water by using titanate nanofibers and nanotubes. Angew. Chemie 123, 10782–10786.

Yeyin, N., Cavdar, I., Uslu, L., Abuqbeitah, M., Demir, M., 2016. Effects of hemodialysis on iodine-131 biokinetics in thyroid carcinoma patients with end-stage chronic renal failure. Nucl. Med. Commun. 37, 283–287.

Yu, F., Chen, Y., Wang, Y., Liu, C., Ma, W., 2018. Enhanced removal of iodide from aqueous solution by ozonation and subsequent adsorption on Ag-Ag2O modified on Carbon Spheres. Appl. Surf. Sci. 427, 753–762.

Yuan, X., Sun, M., Yao, Y., Lin, X., Shi, J., 2019. N/Ti 3 + -codoped triphasic TiO 2/gC 3 N 4 heterojunctions as visible-light photocatalysts for the degradation of organic

contaminants. New J. Chem. 43, 2665–2675.

Zhang, S., Xu, C., Creeley, D., Ho, Y.-F., Li, H.-P., Grandbois, R., Schwehr, K.A., Kaplan, D.I., Yeager, C.M., Wellman, D., 2013. Iodine-129 and iodine-127 speciation in groundwater at the Hanford Site, US: iodate incorporation into calcite. Environ. Sci. Technol. 47, 9635–9642.

Zhang, X., Gu, P., Li, X., Zhang, G., 2017. Efficient adsorption of radioactive iodide ion from simulated wastewater by nano Cu2O/Cu modified activated carbon. Chem. Eng. J. 322, 129–139.

Zhong, K., Feng, J., Gao, H., Zhang, Y., Lai, K., 2019. Fabrication of BiVO4@ g-C3N4 (100) heterojunction with enhanced photocatalytic visible-light-driven activity. J.

Solid State Chem. 274, 142–151.

Zou, Y., Wang, X., Ai, Y., Liu, Y., Ji, Y., Wang, H., Hayat, T., Alsaedi, A., Hu, W., Wang, X., 2016. β-Cyclodextrin modified graphitic carbon nitride for the removal of pollutants from aqueous solution: experimental and theoretical calculation study. J. Mater. Chem. A 4, 14170–14179.

Zou, Y., Wang, P., Yao, W., Wang, X., Liu, Y., Yang, D., Wang, L., Hou, J., Alsaedi, A., Hayat, T., 2017. Synergistic immobilization of UO22+ by novel graphitic carbon nitride@ layered double hydroxide nanocomposites from wastewater. Chem. Eng. J. 330, 573–584.